



## The CU mobile Solar Occultation Flux instrument: structure functions and emission rates of NH<sub>3</sub>, NO<sub>2</sub> and C<sub>2</sub>H<sub>6</sub>

Natalie Kille<sup>1,2</sup>, Sunil Baidar<sup>2,3,a</sup>, Philip Handley<sup>2,3,a</sup>, Ivan Ortega<sup>2,3,b</sup>, Roman Sinreich<sup>3</sup>, Owen R. Cooper<sup>4</sup>, Frank Hase<sup>5</sup>, James W. Hannigan<sup>6</sup>, Gabriele Pfister<sup>6</sup>, and Rainer Volkamer<sup>1,2,3</sup>

<sup>1</sup>Department of Atmospheric and Oceanic Sciences (ATOC), University of Colorado, Boulder, CO, USA

<sup>2</sup>Cooperative Institute for Research in Environmental Sciences (CIRES), University of Colorado, Boulder, CO, USA

<sup>3</sup>Department of Chemistry and Biochemistry, University of Colorado, Boulder, CO, USA

<sup>4</sup>National Ocean Atmosphere Administration (NOAA), Chemical Sciences Division (CSD), Boulder, CO, USA

<sup>5</sup>Institut für Meteorologie und Klimaforschung – Atmosphärische Spurengase und Fernerkundung (IMK-ASF), Karlsruhe Institute of Technology (KIT), Karlsruhe, Germany

<sup>6</sup>National Center for Atmospheric Research (NCAR), Atmospheric Chemistry Observations & Modeling Laboratory (ACOM), Boulder, CO, USA

<sup>a</sup>now at: NOAA/CSD, Boulder, CO, USA

<sup>b</sup>now at: NCAR/ACOM, Boulder, CO, USA

Correspondence to: R. Volkamer (rainer.volkamer@colorado.edu)

Received: 8 June 2016 – Published in Atmos. Meas. Tech. Discuss.: 24 August 2016

Revised: 25 December 2016 – Accepted: 7 January 2017 – Published: 1 February 2017

**Abstract.** We describe the University of Colorado mobile Solar Occultation Flux instrument (CU mobile SOF). The instrument consists of a digital mobile solar tracker that is coupled to a Fourier transform spectrometer (FTS) of 0.5 cm<sup>-1</sup> resolution and a UV-visible spectrometer (UV-vis) of 0.55 nm resolution. The instrument is used to simultaneously measure the absorption of ammonia (NH<sub>3</sub>), ethane (C<sub>2</sub>H<sub>6</sub>) and nitrogen dioxide (NO<sub>2</sub>) along the direct solar beam from a moving laboratory. These direct-sun observations provide high photon flux and enable measurements of vertical column densities (VCDs) with geometric air mass factors, high temporal resolution of 2 s and spatial resolution of 5–19 m. It is shown that the instrument line shape (ILS) of the FTS is independent of the azimuth and elevation angle pointing of the solar tracker. Further, collocated measurements next to a high-resolution FTS at the National Center for Atmospheric Research (HR-NCAR-FTS) show that the CU mobile SOF measurements of NH<sub>3</sub> and C<sub>2</sub>H<sub>6</sub> are precise and accurate; the VCD error at high signal to noise ratio is 2–7 %. During the Front Range Air Pollution and Photochemistry Experiment (FRAPPE) from 21 July to 3 September 2014 in Colorado, the CU mobile SOF instrument measured median (minimum, maxi-

imum) VCDs of 4.3 (0.5, 45) × 10<sup>16</sup> molecules cm<sup>-2</sup> NH<sub>3</sub>, 0.30 (0.06, 2.23) × 10<sup>16</sup> molecules cm<sup>-2</sup> NO<sub>2</sub> and 3.5 (1.5, 7.7) × 10<sup>16</sup> molecules cm<sup>-2</sup> C<sub>2</sub>H<sub>6</sub>. All gases were detected in larger 95 % of the spectra recorded in urban, semi-polluted rural and remote rural areas of the Colorado Front Range. We calculate structure functions based on VCDs, which describe the variability of a gas column over distance, and find the largest variability for NH<sub>3</sub>. The structure functions suggest that currently available satellites resolve about 10 % of the observed NH<sub>3</sub> and NO<sub>2</sub> VCD variability in the study area. We further quantify the trace gas emission fluxes of NH<sub>3</sub> and C<sub>2</sub>H<sub>6</sub> and production rates of NO<sub>2</sub> from concentrated animal feeding operations (CAFO) using the mass balance method, i.e., the closed-loop vector integral of the VCD times wind speed along the drive track. Excellent reproducibility is found for NH<sub>3</sub> fluxes and also, to a lesser extent, NO<sub>2</sub> production rates on 2 consecutive days; for C<sub>2</sub>H<sub>6</sub> the fluxes are affected by variable upwind conditions. Average emission factors were 12.0 and 11.4 gNH<sub>3</sub> h<sup>-1</sup> head<sup>-1</sup> at 30 °C for feedlots with a combined capacity for ~54 000 cattle and a dairy farm of ~7400 cattle; the pooled rate of 11.8 ± 2.0 gNH<sub>3</sub> h<sup>-1</sup> head<sup>-1</sup> is compatible with the upper range of literature values. At this emission rate the NH<sub>3</sub>

source from cattle in Weld County, CO (535 766 cattle), could be underestimated by a factor of 2–10. CAFO soils are found to be a significant source of  $\text{NO}_x$ . The  $\text{NO}_x$  source accounts for  $\sim 1.2\%$  of the N flux in  $\text{NH}_3$  and has the potential to add  $\sim 10\%$  to the overall  $\text{NO}_x$  emissions in Weld County and double the  $\text{NO}_x$  source in remote areas. This potential of CAFO to influence ambient  $\text{NO}_x$  concentrations on the regional scale is relevant because  $\text{O}_3$  formation is  $\text{NO}_x$  sensitive in the Colorado Front Range. Emissions of  $\text{NH}_3$  and  $\text{NO}_x$  are relevant for the photochemical  $\text{O}_3$  and secondary aerosol formation.

## 1 Introduction

Gases emitted from anthropogenic sources can have a profound impact on local air quality (Raga et al., 2001; Ramathan and Feng, 2009) and climate (IPCC, 2013). Emissions from large cattle feedlots contain ammonia ( $\text{NH}_3$ ; Hutchinson et al., 1982; Flesch et al., 2007), which is a precursor for aerosol via the formation of ammonium salts (Walker et al., 2004).  $\text{NH}_3$  is a major source for reactive nitrogen to form particulate matter 2.5 ( $\text{PM}_{2.5}$ ), which negatively affects human health (Todd et al., 2008). Ammonium salts form when  $\text{NH}_3$  reacts with inorganic (Doyle et al., 1979) and organic (Zhang et al., 2004) acids (Fangmeier et al., 1994). Ammonium is mainly present in the submicron fraction of aerosol and contributes significantly to  $\text{PM}_{2.5}$  mass worldwide (Zhang et al., 2007). Aerosol can travel a long distance in the atmosphere before deposition, thus affecting greater regions than the local environment (Hristov et al., 2011). Oil and natural gas (ONG) production is a source for fugitive emissions of ethane ( $\text{C}_2\text{H}_6$ ; Xiao et al., 2008), a small volatile alkane, and volatile organic carbon (VOC) precursor of ozone ( $\text{O}_3$ ; Parrish and Fehsenfeld, 2000). The emissions of  $\text{C}_2\text{H}_6$  from the ONG sector in areas of hydraulic fracturing are highly uncertain and are an area of active research with interest in emission rates, air quality and climate impacts (Ahmadov et al., 2015).  $\text{C}_2\text{H}_6$  contributes to oxidation production of formaldehyde (HCHO) and acetaldehyde ( $\text{CH}_3\text{CHO}$ ; Lou et al., 2007), which is a carcinogen and precursor for radicals that lead to photochemical  $\text{O}_3$  production (Lei et al., 2009; Baidar et al., 2013). HCHO as a radical source also affects the oxidative capacity that is relevant for secondary aerosol formation (Fried et al., 1997; Franco et al., 2015). Nitrogen dioxide ( $\text{NO}_2$ ), emitted during combustion, is a precursor for the formation of photochemical  $\text{O}_3$  (Finlayson-Pitts and Pitts, 2000). Only  $\sim 10\%$  of  $\text{NO}_x$  ( $=\text{NO} + \text{NO}_2$ ) emissions from vehicles is in the form of  $\text{NO}_2$  directly (Carslaw and Beevers, 2005). Another source of  $\text{NO}_x$  are soils from feedlots (Denmead et al., 2008). Based on SCIAMACHY (Scanning Imaging Spectrometer for Atmospheric Cartography) satellite observations, Australia and the Sahara produce  $\text{NO}_x$  predom-

inantly from soil, whereas the United States predominantly produces  $\text{NO}_x$  from anthropogenic sources, such as combustion (Jaeglé et al., 2005; Bertram et al., 2005). Health effects of  $\text{O}_3$  and aerosols require assessment of emissions of the precursor gases. The US Environmental Protection Agency (EPA) recently updated its guidelines for fence-line monitoring to better protect communities near refineries (Jones, 2015).

The Solar Occultation Flux (SOF) method uses direct sunlight to determine vertically integrated concentrations of trace gases (Mellqvist et al., 2010; EPA Handbook, 2011; Johansson et al., 2014b; Kim et al., 2011; European Commission, 2015). The SOF method has been used on mobile platforms to measure ethene (de Gouw et al., 2009; Mellqvist et al., 2010; Johansson et al., 2014a, b), propane (Mellqvist et al., 2010; Johansson et al., 2014a, b) and alkanes including  $\text{C}_2\text{H}_6$  (Johansson et al., 2014b),  $\text{C}_2\text{H}_4$  and  $\text{C}_3\text{H}_6$  (Kim et al., 2011). De Foy et al. (2007) used the SOF method stationary to measure alkanes and  $\text{NH}_3$ , amongst others. However, no reports of  $\text{NH}_3$  currently exist using the SOF method on a mobile laboratory. Column observations integrate over the planetary boundary layer height (PBLH) and hence are independent of its changing height. Column measurements can be used to quantify the emission flux/production rate from an area source by driving around the source or driving upwind and downwind of that source area. The SOF method is complementary to other techniques used to quantify emissions, such as in situ measurements, or stationary deployment of several commercial EM27/SUN Fourier transform spectrometer (FTS) around an area source (Hase et al., 2015; Chen et al., 2016). In situ measurements, or open-path eddy covariance studies (Baum et al., 2008), provide more localized information and require access to the site of interest. Micrometeorological gradient methods require assumptions of homogeneity (Todd et al., 2008). One benefit of mobile SOF measurements is that the total amount is quantified remotely, and no assumptions about homogeneity need to be made. With the mobile SOF a source can be isolated and quantified remotely. The emission flux and source strength is determined by the mass balance approach (Ibrahim et al., 2010; Mellqvist et al., 2010; Baidar et al., 2013).

Structure functions (Follette-Cook et al., 2015) characterize how the variability in vertical column densities (VCDs) changes over distance (see Sects. 2.6 and 3.5). We use the structure function to characterize the VCD variability of  $\text{NH}_3$ ,  $\text{NO}_2$  and  $\text{C}_2\text{H}_6$  on the spatial scale of a satellite ground pixel. Satellites used to retrieve these gases are, for example, the Tropospheric Emission Spectrometer (TES) with a ground pixel size of  $5.3 \times 8.5 \text{ km}^2$  and Infrared Atmospheric Sounding Interferometer (IASI) with a footprint of  $12 \times 25 \text{ km}^2$  for  $\text{NH}_3$  (Shephard et al., 2011; Van Damme et al., 2014; Dammers et al., 2016), the Atmospheric Chemistry Experiment Fourier transform infrared spectrometer (ACE-FTS) and Michelson Interferometer for Passive Atmospheric Sounding (MIPAS) for  $\text{C}_2\text{H}_6$  (Rinsland et al., 2005;

**Table 1.** Specifications of the CU mobile SOF instrument.

Characteristic	Mid-IR		UV-vis
	Channel 1	Channel 2	Channel 3
Spectrometer	Michelson interferometer EM27		Grating spectrometer QE65000
Spectral resolution	0.5 cm <sup>-1</sup>		~0.55 nm
Detector	MCT	InSb	CCD <sup>3</sup>
Spectral range	700–1850 cm <sup>-1</sup>	1850–5000 cm <sup>-1</sup>	390–520 nm
Dimensions <sup>1</sup>	860 mm × 520 mm × 600 mm		
Weight <sup>1</sup>	~45 kg		
Power requirement <sup>2</sup>	115V AC, 380 W		

<sup>1</sup> Includes the solar tracker, spectrometers and base plate. <sup>2</sup> Includes the solar tracker, spectrometers, laptops for data acquisition and control electronics. <sup>3</sup> Charge-coupled device.

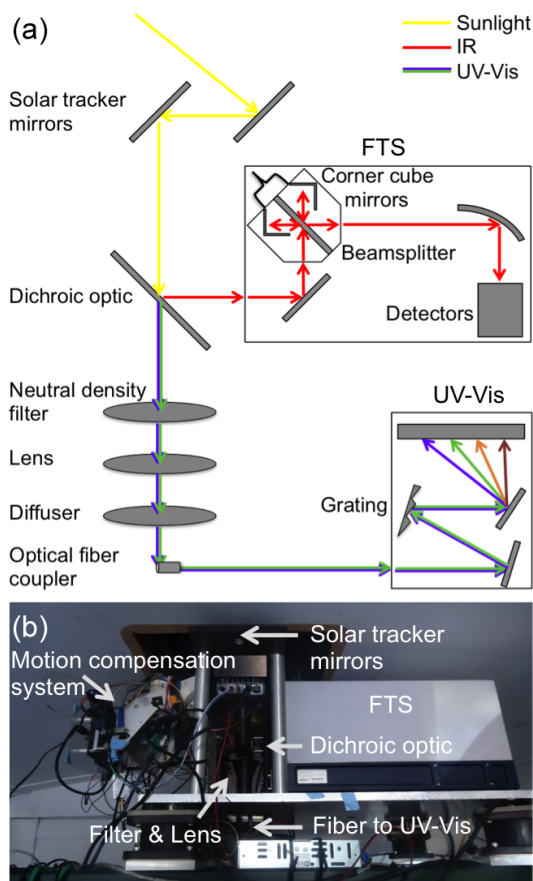


**Figure 1.** (a) Conceptual sketch of the mobile SOF instrument components. (b) Picture of the instrument installed inside the trailer.

Coheur et al., 2007; Fischer et al., 2008; Glatthor et al., 2009; Höpfner et al., 2016), SCIAMACHY with a ground pixel size of  $15 \times 26 \text{ km}^2$  and Ozone Monitoring Instrument (OMI) with a resolution of  $13 \times 24 \text{ km}^2$  for  $\text{NO}_2$  (Boersma et

al., 2009). With their large spatial coverage and continuous global monitoring, satellites have the potential to increase knowledge about the large distribution and cycles of gases. However, satellite observations remain not very well validated (Dammers et al., 2016) and satellites quantifying  $\text{C}_2\text{H}_6$  VCDs are not sensitive to the lower troposphere (Streets et al., 2013). Previous satellite comparisons have used mobile in situ measurements of  $\text{NH}_3$  to characterize the near-surface  $\text{NH}_3$  mixing ratio variability in the San Joaquin Valley in California and compare with data from TES (Sun et al., 2015a) and CrIS (Cross-track Infrared Sounder) satellites (Shepherd and Cady-Pereira, 2015). To our knowledge there currently is no attempt to characterize the sub-satellite ground pixel variability using mobile VCD observations of  $\text{NH}_3$  and  $\text{C}_2\text{H}_6$ . Mobile VCD measurements eliminate the need for assumptions about  $\text{NH}_3$  and  $\text{C}_2\text{H}_6$  vertical distributions.

## 2 Experimental design

The University of Colorado (CU) digital mobile solar tracker (Baidar et al., 2016), with an integrated motion compensation system and imaging feedback loop, operates autonomously and tracks the sun at high precision. Here, this tracker was coupled to a moderate resolution  $0.5 \text{ cm}^{-1}$  FTS optimized for fast measurements of spectra in the mid-infrared (mid-IR) spectral range. The CU mobile SOF instrument components are shown in Fig. 1 and further specified in Table 1. Figure 1 shows that photons along the direct solar beam are reflected by a set of two mirrors in the solar tracker. A dichroic optic separates the IR from the ultraviolet–visible (UV–vis) wavelengths and directs the beam towards the FTS. The UV–vis wavelengths continue through several optics before entering the optical fiber coupler directing the beam into the UV–vis grating spectrometer. The FTS has two channels and the UV–vis spectrometer has one channel (see Table 1). The instru-

mentation was mounted inside a trailer with the solar tracker placed through the roof of the trailer.

## 2.1 Digital mobile solar tracker

The digital mobile solar tracker has been described in detail elsewhere (Baidar et al., 2016). In brief, it consists of a set of planar aluminum mirrors; one mirror is mounted directly on the axis of a stepper motor regulating the elevation angle and one is on a rotation stage regulating the azimuth angle. The mirrors are controlled from an embedded computer system (PC104) that is integrated with a motion compensation system to calculate the Euler angles of the sun for coarse tracking and a real-time imaging feedback loop for fine tracking. During mobile deployment the solar tracker has a demonstrated angular precision of  $0.052^\circ$  and allows the reliable tracking of the sun even on uneven dirt roads from a moving mobile laboratory. This tracking precision and first trace gas measurements have been demonstrated using the center to limb darkening (CLD) of solar Fraunhofer lines and  $\text{NO}_2$  lines at UV–vis wavelengths. The direct-sun differential optical absorption spectroscopy (DS-DOAS)  $\text{NO}_2$  VCDs have further been compared to  $\text{NO}_2$  VCDs measured by MAX-DOAS (multi-axis DOAS; Baidar et al., 2016). Here, we describe the addition of an FTS to simultaneously measure trace gases at mid-IR wavelengths.

## 2.2 Mobile SOF EM27 FTS

A customized Bruker EM27 FTS was characterized for the use from mobile platforms coupled to the solar tracker, see Fig. 1. The EM27 FTS is a Michelson interferometer with a double pendulum corner cube mirror design. The oscillating mirrors determine the optical path difference (OPD). Our configuration allows for fast scanning at 160 kHz to provide spectra acquisition with 2 Hz time resolution and includes a zinc selenide (ZnSe) beam splitter and window, 24 V power supply and a Stirling-cooled sandwich detector operating at 77 K, consisting of a mercury cadmium telluride (MCT) and an indium antimonide (InSb) detector in a single detector housing. Each detector has an active area of 1 mm diameter. The FTS allows for measurements over a wide spectral range in the mid-IR spectral region of the solar spectrum from 700 to  $5000\text{ cm}^{-1}$ . We did not use an apodization function for the measurements during FRAPPE. Boxcar was selected in order to keep the resolution at its maximum of  $0.5\text{ cm}^{-1}$ . Further specifications about the instrument configuration are provided in Table 1.

The instrument characterization is described in Sect. 2.4.

### 2.2.1 $\text{NH}_3$ and $\text{C}_2\text{H}_6$ retrieval

The spectra taken with the MCT detector were corrected for instrument background. An example solar spectrum measured by the MCT and InSb detectors is shown in Fig. 2, where the micro windows used for the  $\text{C}_2\text{H}_6$  and  $\text{NH}_3$  re-

**Table 2.** Spectral fit windows used in the retrievals.

Target species	Interfering species	Spectral range
$\text{NH}_3$	$\text{O}_3, \text{H}_2\text{O}, \text{CO}_2, \text{C}_2\text{H}_4$	$950\text{--}980\text{ cm}^{-1}$
$\text{C}_2\text{H}_6$	$\text{CH}_3\text{Cl}, \text{H}_2\text{O}, \text{HDO}, \text{CH}_4$	$2970\text{--}3000\text{ cm}^{-1}$
$\text{NO}_2$	$\text{O}_3, \text{H}_2\text{O}, \text{O}_4, \text{C}_2\text{H}_2\text{O}_2, \text{CLD}$	$434\text{--}460\text{ nm}$

trieval are highlighted with yellow bars.  $\text{NH}_3$  VCDs were retrieved from MCT spectra using the micro window  $950\text{--}980\text{ cm}^{-1}$ . The InSb spectra were used without further corrections for the retrieval of  $\text{C}_2\text{H}_6$  at  $2970\text{--}3000\text{ cm}^{-1}$ . The spectral fit windows including interfering species are listed in Table 2. All retrievals were conducted using the SFIT4 software (Hase et al., 2004; Nussbaumer and Hannigan, 2014) and a priori profile parameters as given in Table 3. SFIT4 uses the vertical profiles of pressure, temperature and water vapor taken from NCEP (National Centers for Environmental Prediction) and WACCM (Whole Atmosphere Community Climate Model, <https://www2.acom.ucar.edu/gcm/waccm>) at given altitudes that were assumed to be constant throughout each day. It uses updated  $\text{C}_2\text{H}_6$  lines from Harrison et al. (2010) and HITRAN 2008 (Rothman et al., 2009) line lists for all other absorbers listed in Table 2. The a priori error allows for the VCD of interest ( $\text{NH}_3$  or  $\text{C}_2\text{H}_6$ ) to vary by a factor of 100 around the a priori value; the interfering gases, e.g.,  $\text{CO}_2$  and  $\text{H}_2\text{O}$ , were allowed less variability. SFIT iterates to obtain a best fit between the calculated and measured spectrum. The residual parameter (%rms) is used to quality assure our data. The quality assurance cutoff %rms value has been determined by contrasting  $\frac{1}{\sqrt{N}}$  noise against the residual, where  $N$  is the cumulative number of spectra that have a %rms less than or equal to the threshold, and noise is the spread of residuals within the threshold. The cutoff %rms has been taken as 3 times the minimum of the  $\frac{1}{\sqrt{N}}$  noise against the residual plot and was determined to be 3.6 for  $\text{NH}_3$  and 6.4 for  $\text{C}_2\text{H}_6$ . This translates to  $\sim 75\%$  of  $\text{NH}_3$  and  $\sim 47\%$  of  $\text{C}_2\text{H}_6$  spectra being considered during analysis. Spectral proof of the detection of both gases is shown in Fig. 2. In that shown case the detected gas column density of  $\text{C}_2\text{H}_6$  has a value of  $7.13 \times 10^{16}\text{ molecules cm}^{-2}$  and for  $\text{NH}_3$  a value of  $40.2 \times 10^{16}\text{ molecules cm}^{-2}$ , which is well above the detection limit (see Sect. 3.1.1). The top panel of the fit window shows the residual between observed and fitted spectrum. Besides the observed and fitted spectrum the fit window also includes the strongest interfering trace gases.

## 2.3 UV–vis spectrometer

The UV–vis channel consists of an OceanOptics QE65000 grating spectrometer to measure  $\text{NO}_2$  VCDs. The spectrometer has a charge-coupled device detector covering the spec-

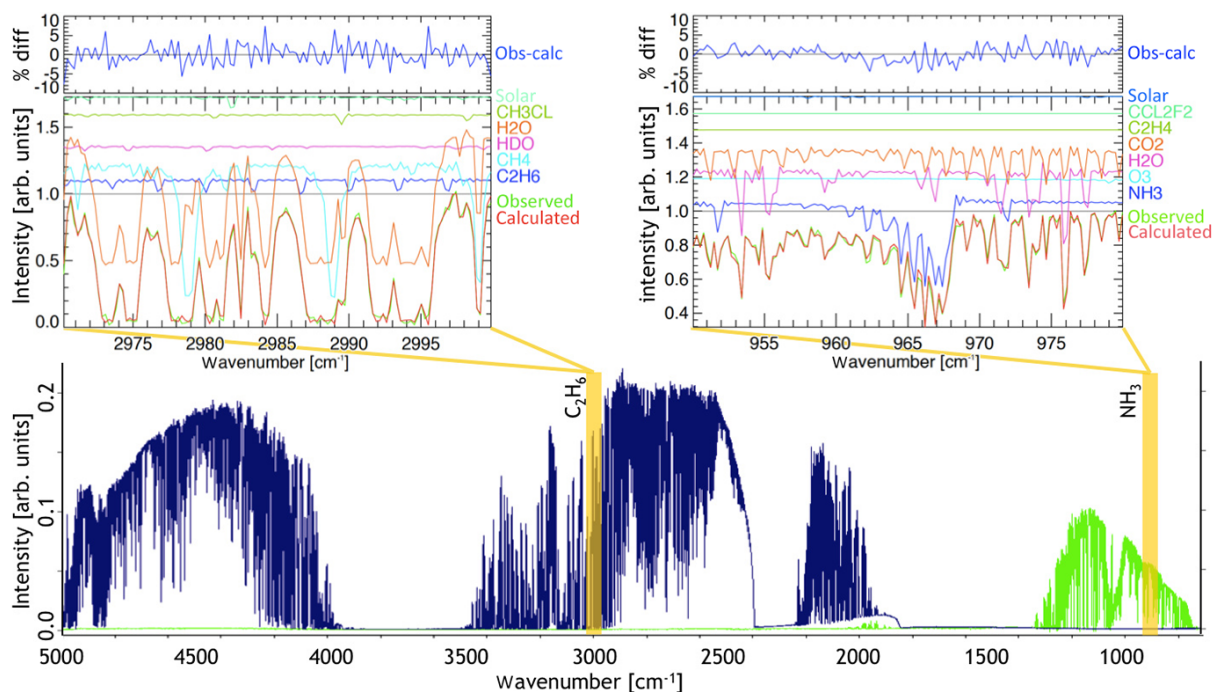


**Figure 2.** Solar spectrum measured by the InSb (blue) and MCT (green) detectors. Yellow bars indicate the spectral intervals used for the retrieval of  $\text{C}_2\text{H}_6$  and  $\text{NH}_3$ . Spectral proof of  $\text{C}_2\text{H}_6$  is shown on the top left and of  $\text{NH}_3$  on the top right. The  $\text{C}_2\text{H}_6$  column was  $7.13 \times 10^{16}$  molecules  $\text{cm}^{-2}$  (%rms = 2.7) and the  $\text{NH}_3$  column was  $40.2 \times 10^{16}$  molecules  $\text{cm}^{-2}$  (%rms = 1.9) for the retrievals shown.

**Table 3.** Overview of SFIT4 a priori values.

Species	A priori (molec $\text{cm}^{-2}$ )	A priori error (%)
$\text{C}_2\text{H}_6$	$1.18 \times 10^{16}$	10000
$\text{NH}_3$	$2.23 \times 10^{13}$	10000
$\text{CH}_3\text{Cl}$	$8.88 \times 10^{15}$	1000
$\text{H}_2\text{O}$	$3.78 \times 10^{22}$	50
$\text{HDO}$	$1.43 \times 10^{23}$	50
$\text{CH}_4$	$3.12 \times 10^{19}$	100
$\text{O}_3$	$8.44 \times 10^{18}$	1
$\text{C}_2\text{H}_4$	$3.75 \times 10^{14}$	10
$\text{CO}_2$	$6.65 \times 10^{21}$	10

tral range 390–520 nm as is described elsewhere (Baidar et al., 2016).

### 2.3.1 $\text{NO}_2$ retrieval

$\text{NO}_2$  was measured by the UV–vis spectrometer using the retrievals described in Baidar et al. (2016). In brief,  $\text{NO}_2$  was retrieved in the spectral fitting window 434–460 nm using the WinDOAS software (Van Roozendaal and Fayt, 2001). Baidar et al. (2016) also have compared the DS-DOAS  $\text{NO}_2$  VCDs with MAX-DOAS to assess benefits of high photon fluxes for sensitivity and validate the  $\text{NO}_2$  measurements.

## 2.4 Mobile SOF characterization

### 2.4.1 Comparison at NCAR

Prior to field deployment, collocated measurements were performed with the mobile laboratory at the National Center for Atmospheric Research (NCAR) in Boulder, CO, with a high-resolution Bruker 120HR FTS (HR-NCAR-FTS). The CU mobile SOF instrument was mounted in a trailer that was parked in the parking lot  $\sim 50$  m away from the HR-NCAR-FTS, assuring that both instruments observed the nearly same air mass. Coincident time intervals of the measurements were evaluated to determine the accuracy of the trace gas VCDs and the limit of detection (LOD) of the  $0.5 \text{ cm}^{-1}$  resolution FTS. We calculate the LOD using the following IUPAC definition (IUPAC, 2006):

$$\text{LOD}_{\text{exp}} = k \cdot \sigma_{\text{Gaussian}} + |\text{background}|, \quad (1)$$

where  $k$  is a factor chosen according to the confidence interval, and  $\sigma_{\text{Gaussian}}$  is the standard deviation during a time period in which the air mass is not changing (i.e., constant  $\text{C}_2\text{H}_6$  and  $\text{NH}_3$  VCD). We set  $k = 3$  for a 99.7% confidence interval. Here, the LOD is given in units of VCD and determines the minimum amount of a gas to be detected in order to be statistically distinct from a blank measure (Long and Winefordner, 1983; Schrader, 1995). In the mornings before a research drive (RD) and, if the cloud cover permitted, in the afternoon after an RD, stationary measurements were

**Table 4.** Results of the FTS quality assurance.

	Channel 1 /NH <sub>3</sub>	Channel 2 /C <sub>2</sub> H <sub>6</sub>
Precision <sup>1</sup> (10 <sup>16</sup> molec cm <sup>-2</sup> )	0.01	0.01
Accuracy <sup>2</sup> (10 <sup>16</sup> molec cm <sup>-2</sup> )	0.07	0.10
LOD (10 <sup>16</sup> molec cm <sup>-2</sup> )	<b>0.10</b>	<b>0.13</b>
Total error (%)	<b>4.4</b>	<b>6.7</b>
OPD effect <sup>3</sup> (%) (2σ)	1.0	0.0
Cross section uncertainty (%)	2.0 <sup>4</sup>	4.0 <sup>5</sup>
Fit uncertainty (%) (2σ)	3.8	5.4

<sup>1</sup> Calculated as the mean during periods in which the atmosphere remained constant. <sup>2</sup> Calculated as the difference between the CU mobile lab FTS and the NCAR high-resolution FTS. <sup>3</sup> Calculated for a median VCD of  $4.32 \times 10^{16}$  molec cm<sup>-2</sup> for NH<sub>3</sub> and  $3.49 \times 10^{16}$  molec cm<sup>-2</sup> for C<sub>2</sub>H<sub>6</sub> as measured during RD10 and RD11. <sup>4</sup> Source: Kleiner et al. (2003). <sup>5</sup> Source: Harrison et al. (2010).

taken in a parking lot at CU (40.005°N, 105.270°W) to determine  $\sigma_{\text{Gaussian}}$ , and they were found to be consistent with the  $\sigma_{\text{Gaussian}}$  determined at NCAR shown in Fig. 3. The figure shows the VCD measurements of NH<sub>3</sub> and C<sub>2</sub>H<sub>6</sub> from the HR-NCAR-FTS in blue and mobile SOF data in black. Mobile SOF VCD measurements were taken at specific integration times. A longer integration time averages more scans and reduces the noise in the data. For the background determination mobile SOF data points within the integration time of one HR-NCAR-FTS were averaged. The background was calculated as the difference between mobile SOF FTS and HR-NCAR-FTS data points. See Sect. 3.1.1 for discussion on the comparison.

## 2.4.2 Characterization of the ILS

For measurements from the mobile laboratory the azimuth and elevation angles change rapidly over the course of an RD. It is therefore important to characterize the ILS (Hase et al., 1999) over a wide range of azimuth and elevation angle pairs. This was tested in a laboratory setup where the solar tracker was pointed at a globar to observe atmospheric water vapor over a distance of several meters along the path between the FTS and the globar. The light emitted by the globar is collimated and directed onto the solar tracker. The FTS with solar tracker is positioned on a rotatable platform. The ILS has been determined using the retrieval code LINEFIT (Hase et al., 1999) version 14 using water vapor absorption lines in the spectral range at 1950–1900 for the InSb and at 1820–1800 cm<sup>-1</sup> for the MCT detector. The modulation efficiency at maximum OPD is shown in Fig. 4 for different azimuthal and elevation angles, and the results are further discussed in Sect. 3.1.2 and Table 4.

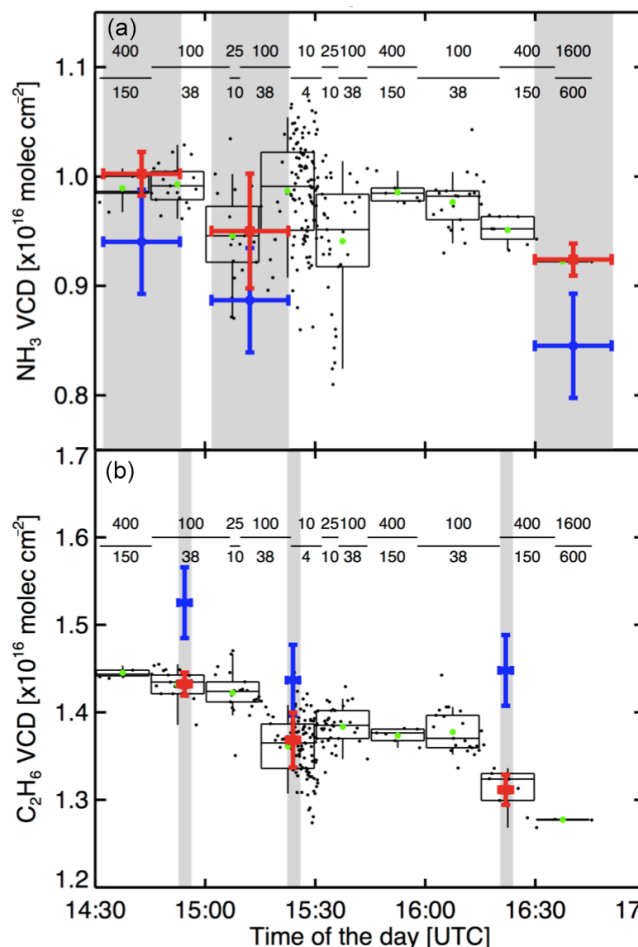


**Figure 3.** Assessment of CU mobile SOF accuracy at NCAR, Boulder, CO: (a) NH<sub>3</sub> and (b) C<sub>2</sub>H<sub>6</sub>. Blue: measurements of the HR-NCAR-FTS; black: individual mobile SOF measurements (variable integration time); red: mobile SOF data averaged over the time period of the NCAR measurements (indicated in grey); green: 15 min averages of mobile SOF data. The dashes indicate during which time period the individual mobile SOF measurements were taken. Numbers above the dashes indicate the internally co-added scan number and numbers below indicate the integration time of each stored spectrum in seconds. Boxes and whiskers represent 5th, 25th, median, 75th and 95th percentiles for every 15 min. The VCD uncertainty on the mobile SOF and NCAR measurements is given as the  $1\sigma$  standard deviation.

## 2.5 Flux calculations

VCD measurements around a site of interest were used in combination with wind fields to calculate the emission flux using the mass balance approach (Ibrahim et al., 2010; Melqvist et al. 2010; Baidar et al., 2013). The flux is calculated from the following equation:

$$\text{NetFlux} = \int_S \text{VCD} \vec{F} \cdot \vec{n} \, ds, \quad (2)$$

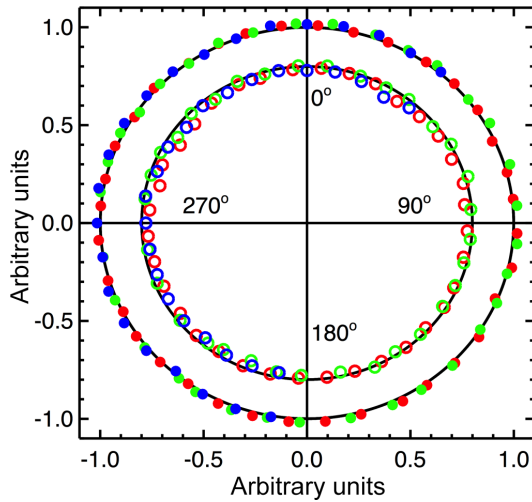


**Figure 4.** Angle dependence of the instrument line shape (ILS) modulation efficiency at maximum OPD. MCT detector: open circles. InSb detector: filled circles. Green, red and blue measured at an elevation angle of 5, 45 and 65°, respectively. The black unit circles represent an ideal ILS modulation efficiency having a value of 1.000. See text for details.

where VCD is the vertical column density,  $\vec{F}$  is the wind vector,  $\vec{n}$  is the outward facing normal with respect to the driving direction, and the integral over  $ds$  represents the drive track around a closed box. In order to determine the emission flux or production rate of a gas the wind vector needs to be known.

### 2.5.1 Uncertainty due to the model winds

We use model wind to perform the flux calculations. The model wind, extracted from the North American Mesoscale Model using the National Emission Inventory 2011 version 2 (NAM, NEI 2011v2) and with inner domain of 4 km, was interpolated for hourly instantaneous values at 36 altitudes from ~ 10–50 m above ground to ~ 18.5 km along the exact drive track coordinate and time.

The model wind was compared to measurements of wind speed and direction at the Boulder Atmospheric Observatory (BAO), observed at 10, 100 and 300 m above ground; Fig. 6 shows where the BAO tower is located. The uncertainty analysis of the model wind speed and wind direction is based on the time window 16:00–22:00 UTC, which is the time spent on the RDs. The model wind did not exactly have altitude layers at 10, 100 and 300 m to compare to BAO; therefore, the model wind was extracted at 3, 105 and 325 m, respectively, which represent the values closest to the BAO tower altitudes. The results are shown in Fig. S1 in the Supplement.

The error component due to wind direction was actively minimized using the spatial information contained in the mobile SOF data. The wind direction is constrained by the direction of the plume evolution from the sites and measure-

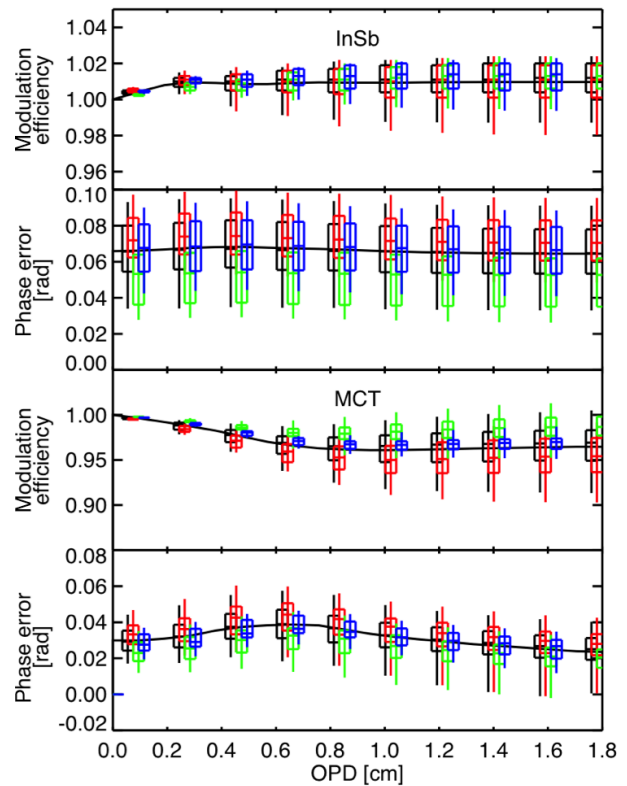


**Figure 5.** Instrument line shape (ILS) modulation efficiency and phase error as a function of optical path difference (OPD). Top panels: InSb detector. Bottom panels: MCT detector. Boxes mark 25th and 75th percentiles, and the line inside the box marks the median. Lines outside the boxes indicate 5th and 95th percentile. Green, red and blue represent averages over an elevation angle of 5, 45 and 65°, respectively. Black is the average over all data. The different colored whiskers are offset with respect to the OPD for visualization; green whiskers are located at the exact OPD.

ments of VCD column enhancements downwind. It was determined that the model wind direction for site 1 is representative of the actual wind direction, whereas for sites 2 and 4 the wind direction was corrected by 7/23 and 11/18° for RD10/RD11, respectively. For comparison, the wind direction at BAO agrees to < 40° on 12 and 13 August 2014. To determine the effect the wind direction uncertainty has on the emission flux, the emission flux was first calculated using the model wind and then compared to the model wind corrected by direction. The bias on the emission flux due to wind direction is  $9.3 \pm 3.6\%$  for site 2 and  $19.0 \pm 8.6\%$  for site 4. This bias has been corrected as described above. For the three sites is the correction leads on average to a  $9.5 \pm 7.8\%$  change in the emission flux.

Based on the slopes in Fig. S1 the wind speed has a percent error of 16.8. There is little variability in the relative differences between measured and predicted wind speed with altitude at BAO, variations are within a few percent. The uncertainty in the emission flux due to the model wind speed

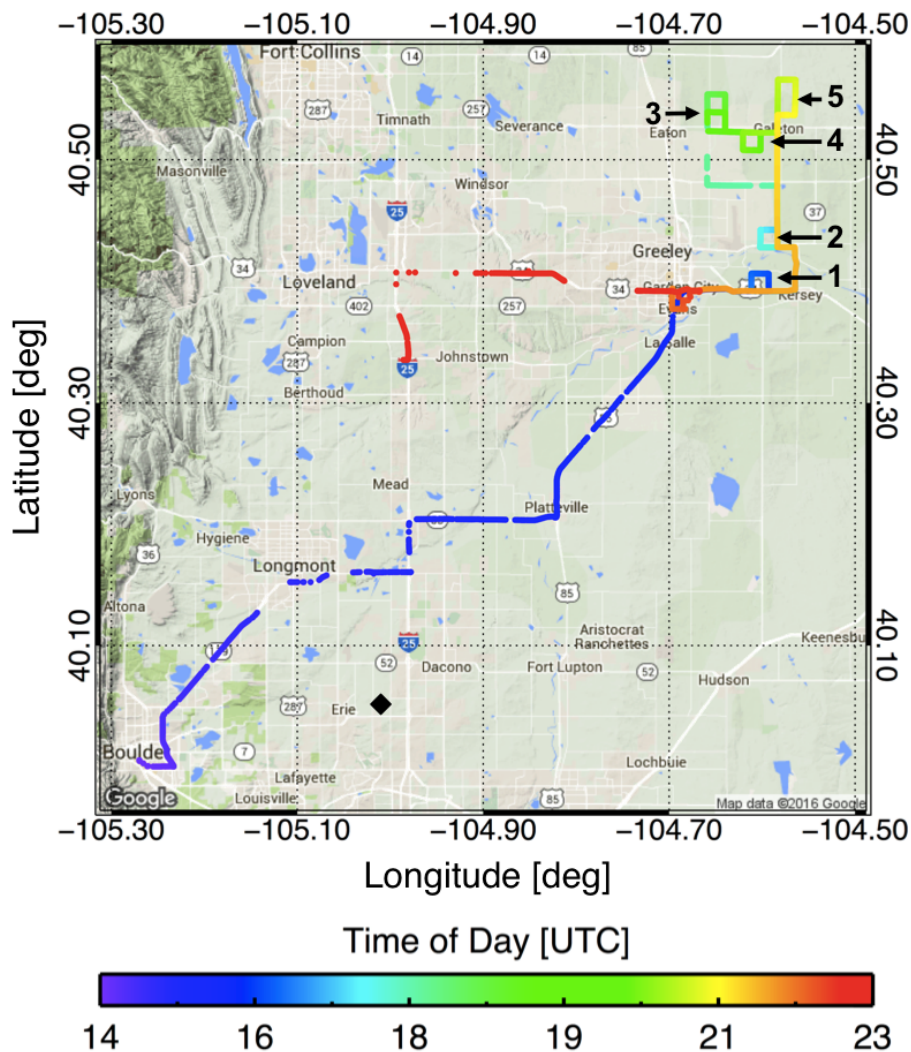


**Figure 6.** Research drive track of RD11 to investigate agricultural sources near Greeley, CO. Sites 1, 4 and 5 are dairy farms, 2 is a beef farm and 3 is a sheep farm. The diamond indicates the location of the BAO tower.

was taken as the average difference over the three altitudes within the PBLH, as indicated in the bottom panel of Figs. 7 and S2.

Vertical plume dispersion determines which altitude to use for averaging the model wind speed. The PBLH varies from  $\sim 500$  to 2500 m from the time of driving around site 1 to site 4. The model estimates that most  $\text{NH}_3$  is located in the lowest 500 m of the VCD. The error due to vertical variability in winds during RD10 and RD11 was  $11.2 \pm 8.3\%$ . This error falls within the error on wind speed, indicating that the emission flux here is not sensitive to the vertical plume extend.

The combined uncertainty of wind direction and wind speed on the emission flux is 18 % for site 1 during both RD10 and RD1 and dominated by the error in the wind speed. For site 2 the total wind uncertainty on emission flux is  $17.8 \pm 0.5\%$ , and for site 4 the uncertainty is  $22.0 \pm 3.4\%$ . Based on the evaluation of winds at BAO, and use of the

corrected wind direction for each site, the uncertainty in the emission fluxes due to winds is 20 %.

### 2.5.2 Overall uncertainty in the emission fluxes

The overall uncertainty in the emission fluxes combines the uncertainty of the trace gas VCD measurements (see Table 4) and the model winds. Section 3.1 describes in detail the error of the VCD measurements. For all gases the error of the trace gas VCD is about a factor 4 smaller than the error due to model winds in the flux calculation (see Eq. 2). The  $\text{NH}_3$ ,  $\text{NO}_2$  and  $\text{C}_2\text{H}_6$  fluxes and the respective overall flux uncertainties calculated from combining the error in the VCD measurements and model winds are shown in Sect. 3.3, Table 5 and the Supplement.

**Table 5.** NH<sub>3</sub>, NO<sub>2</sub> and C<sub>2</sub>H<sub>6</sub> flux estimates from 12 August (RD10) and the case study on 13 August 2014 (RD11). The uncertainty on the fluxes is assuming the model wind has an uncertainty of 20 %.

Site	1	2	4
Size (km × km)	1.6 × 1.6	1.6 × 1.6	1.6 × 1.6
Source type	Dairy	Beef	Dairy
Maximum count <sup>1</sup>	unknown	54 044	7450
NH <sub>3</sub> flux (kg h <sup>-1</sup> ) – RD10	128 ± 26	625 ± 128	85 ± 17
NH <sub>3</sub> flux (kg h <sup>-1</sup> ) – RD11	89 ± 18	673 ± 138	NN <sup>2</sup>
NO <sub>2</sub> flux (kg h <sup>-1</sup> ) – RD10	NN <sup>2</sup>	18 ± 4	1.3 ± 0.3
NO <sub>2</sub> flux (kg h <sup>-1</sup> ) – RD11	NN <sup>2</sup>	11 ± 2	-2.5 ± 0.5 <sup>3</sup>
C <sub>2</sub> H <sub>6</sub> flux (kg h <sup>-1</sup> ) – RD10	37 ± 8 <sup>3</sup>	NN <sup>2</sup>	NN <sup>2</sup>
C <sub>2</sub> H <sub>6</sub> flux (kg h <sup>-1</sup> ) – RD11	90 ± 19 <sup>3</sup>	NN <sup>2</sup>	NN <sup>2</sup>

<sup>1</sup> Source: CDPHE (Colorado Department of Public Health and Environment); CAFO locations and maximum capacities for FRAPPE (D. Bon, 2016, personal communication). <sup>2</sup> NN indicates no number; significant influence from upwind sources precludes quantification.

<sup>3</sup> Influence from upwind sources is non-negligible.

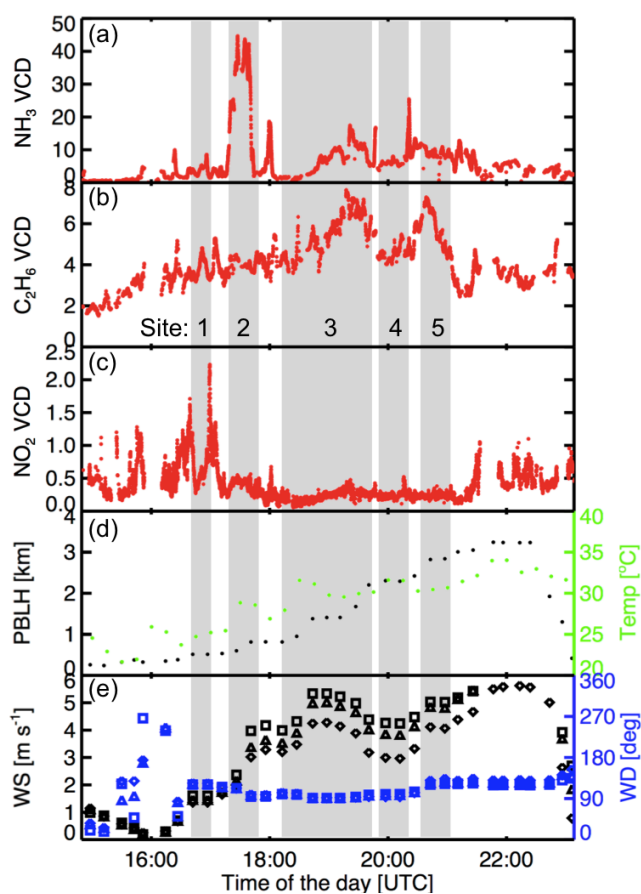


**Figure 7.** Time series of the VCDs ( $10^{16}$  molec  $\text{cm}^{-2}$ ) measured for (a) NH<sub>3</sub>, (b) C<sub>2</sub>H<sub>6</sub> and (c) NO<sub>2</sub> during RD11. (d) PBLH and temperature. (e) Model wind speed and model wind direction averaged over approximately 10–50 m above ground level (diamonds), over half PBLH (triangles) and over the full PBLH (squares). Shaded areas indicate times at each site (numbers correspond to those in Fig. 6).

## 2.6 Structure Function

The structure function to assess the spatial scales of VCD variability is defined as

$$f(Z, y) = \langle |Z(x+y) - Z(x)|^q \rangle, \quad (3)$$

where  $\langle \rangle$  denotes the average difference in VCD within distance  $y$ ,  $Z$  is the VCD of a gas of interest, and  $q$  is a scaling exponent (Harris et al., 2001; Follette-Cook et al., 2015). Setting  $q$  equal to 1 this structure function is a useful tool to quantify trace gas variability over horizontal distance. At small distances between measurements the structure function exhibits the largest rate of change and increases until converging at larger distances. Variabilities increase as both plumes and background air masses are observed. At a certain spatial distance the structure function converges against a maximum VCD variability. We define the variability length scale to determine over which spatial scales a certain percentage of the maximum median variability is observed. The spatial distance at which the VCD variability is 50 % of the maximum variability is denoted as  $L_V$  (50 %). Then

$$L_V(P) = d(P \cdot V_{\max}), \quad (4)$$

where  $L_V$  denotes the variability length scale for a certain percentage  $P$  and  $d(P \cdot V_{\max})$  denotes the distance in kilometers at which the VCD variability equals  $P \cdot V_{\max}$ . Here,  $V_{\max}$  is the maximum median variability.

Figure 9 shows the structure function with units of distance in kilometers on the abscissa, VCD difference has units of molecules  $\text{cm}^{-2}$  on the ordinate, and a second ordinate scales the VCD difference with respect to the median VCD.

## 3 Results and discussion

### 3.1 Mobile SOF performance

#### 3.1.1 Precision and accuracy

The LOD and precision of NO<sub>2</sub> from the DS-DOAS are  $7 \times 10^{14}$  and  $3 \times 10^{14}$  molecules  $\text{cm}^{-2}$ , respectively (Baidar et al., 2016). Figure 3 illustrates the data used to determine the LOD and accuracy of the CU mobile SOF. The absolute values of the difference between the VCDs averaged over identical time intervals measured by the HR-NCAR-FTS and by the mobile SOF were used to quantify accuracy. The results are presented in Table 4. The findings for measurement precision and accuracy (compare Sect. 2.4, Eq. 1) result in the following LODs:  $\text{LOD}_{\text{NH}_3} = 0.10 \times 10^{16}$  molecules  $\text{cm}^{-2}$  and  $\text{LOD}_{\text{C}_2\text{H}_6} = 0.13 \times 10^{16}$  molecules  $\text{cm}^{-2}$ . The accuracy is composed of uncertainty in the cross section, the error associated with the spectral fit and the uncertainty on the retrieved VCD due to the ILS effect (see Sect. 3.1.2). With an accuracy of 6.1 % for NH<sub>3</sub> and 9.0 % for C<sub>2</sub>H<sub>6</sub> and

the above given LOD values this means that the accuracy is limiting the overall uncertainty in trace gas observations at concentrations greater than  $2.27 \times 10^{16}$  for  $\text{NH}_3$  and  $1.94 \times 10^{16}$  molecules  $\text{cm}^{-2}$  for  $\text{C}_2\text{H}_6$ . During FRAPPE, the VCDs were greater than the LOD in 99.98 % for  $\text{NH}_3$  and 100 % for  $\text{C}_2\text{H}_6$  of the measurements, which means the LOD was an issue in a low amount of measurements. In terms of the total error (see Table 4), this means that the uncertainty was determined by the accuracy of the observed median and maximum and the LOD was limiting the uncertainty on the minimum observed VCD. For a median VCD of  $4.32 \times 10^{16}$  molecules  $\text{cm}^{-2}$  for  $\text{NH}_3$  the uncertainty is  $0.19 \times 10^{16}$  molecules  $\text{cm}^{-2}$ , and for a median VCD of  $3.49 \times 10^{16}$  molecules  $\text{cm}^{-2}$  for  $\text{C}_2\text{H}_6$  the uncertainty is  $0.23 \times 10^{16}$  molecules  $\text{cm}^{-2}$ .

### 3.1.2 Instrument line shape

While driving around a source area or site of interest there are  $90^\circ$  changes in the azimuth angle with each turn and many smaller degree changes in both elevation and azimuth angles due to fine tracking on uneven dirt roads. Column density measurements along the  $\sim 2.0$  m long beam between the collimated light source of a gobar and the spectrometer at solar tracker azimuth angles from  $0$  to  $360^\circ$  and at elevation angles of  $5$ ,  $45$  and  $65^\circ$  were recorded to determine the ILS based on water vapor lines (compare Sect. 2.6). Figure 4 shows the modulation efficiency at maximum OPD as a function of azimuth angle. The inner circle shows the measurements for the MCT detector; the outer circle shows the measurements for the InSb detector. Figure 5 shows both the modulation efficiency and phase error as a function of OPD. The top plots show the InSb results; the bottom plots show the MCT results. It can be seen that the modulation efficiency of both detectors shows rather constant behavior. From these experiments it was determined that the MCT detector has a modulation efficiency of 0.968 at maximum OPD and the InSb detector has a modulation efficiency of 1.010 at maximum OPD. These values are obtained by averaging the modulation efficiency at maximum OPD over all azimuth and elevation angle.

To investigate the effect of the ILS on the retrieval of  $\text{NH}_3$  and  $\text{C}_2\text{H}_6$ , the retrieval software was first run using an ideal ILS as input and then using the ILS measured for the MCT and InSb detector, respectively, and comparing the VCD output with ideal and measured ILS. There was 0.5 % change in the retrieved  $\text{NH}_3$  VCD and no change in the  $\text{C}_2\text{H}_6$  VCD. These results are listed in Table 4 and are factored into the total error on VCDs. We conclude that there is no significant angular dependency on the ILS.

### 3.2 Mobile SOF deployment

The mobile SOF was deployed during 16 RDs during FRAPPE. Here, we present data from two RDs that were

conducted along almost identical drive tracks on consecutive days as well as shared common scientific objectives. The drive track for the case study from 13 August 2014 is shown in Fig. 6 and is similar to the drive track on 12 August 2014. The five sites indicated in that figure contain feedlots (and probably ONG storage tanks). On 12 and 13 August 2014, RD10 and RD11, respectively, the following median (minimum, maximum) VCDs were observed: 4.3 (0.5, 45) for  $\text{NH}_3$ , 3.5 (1.5, 7.7) for  $\text{C}_2\text{H}_6$  and 0.4 (0.06, 2.2)  $\times 10^{16}$  molecules  $\text{cm}^{-2}$  for  $\text{NO}_2$ .

The variability in total column densities during RD11 is shown in Figs. 7 and 8. The identical figures for RD10 are included as Figs. S2 and S3. Both RDs show similar features in VCD enhancement ( $\text{VCD} - \text{VCD}_{\text{background}}$ ) of the gases, temperature and wind. Figure 7 shows the VCD time series of the three gases, a time series for the temperature and PBLH, and the model wind speed and direction.  $\text{NH}_3$  shows significant column enhancement for site 2, which was the concentrated animal feeding operation (CAFO) with  $\sim 54\,000$  cattle.  $\text{NO}_2$  also shows some VCD enhancement for site 2. Figure 8 shows the VCD time series in form of a Google Earth visualization to indicate the spatial distribution. Sites 1 and 2 are also shown enlarged to visualize the downwind and upwind effects. Site 1 is a source for both  $\text{NH}_3$  and  $\text{C}_2\text{H}_6$ . There is a dairy farm located near the west end of the site and a source for  $\text{C}_2\text{H}_6$  in the upper right of the site. The VCD enhancement of  $\text{NO}_2$  at the south leg of the site is due to heavy traffic on that street. Site 2 for  $\text{NH}_3$  shows the column enhancement downwind of the cattle feedlot and a background VCD upwind of the cattle feedlot. For that same site  $\text{NO}_2$  shows a larger column enhancement downwind than upwind.  $\text{C}_2\text{H}_6$  is mostly transported through site 2, as can be seen in that the VCD is on the same color scale upwind and downwind of site 2.

### 3.3 Emission fluxes

The emission fluxes were calculated according to Eq. (2) described in Sect. 2.5. The wind used for flux calculations has been averaged within the planetary boundary layer (see Fig. 7). Figure 8c and e show the flux as time series for each site. The stretch downwind of a site shows positive flux values if the site is a source. If the site is not a source, and a gas is passing through the site, then the absolute value of negative incoming flux and positive outgoing flux are expected to be comparable.

The calculated net fluxes are presented in Table 5 for RD10 and RD11. Particularly we could verify that cattle and dairy farms in sites 1, 2 and 4 are significant sources for  $\text{NH}_3$  and that the CAFO soil in site 2 is a significant source of  $\text{NO}_x$ , which we observed in terms of a positive  $\text{NO}_2$  production rate. The numbers in Table 5 reflect the uncertainty of the spectroscopic data and the wind data. The error due to the atmospheric variability is not accounted for explicitly in

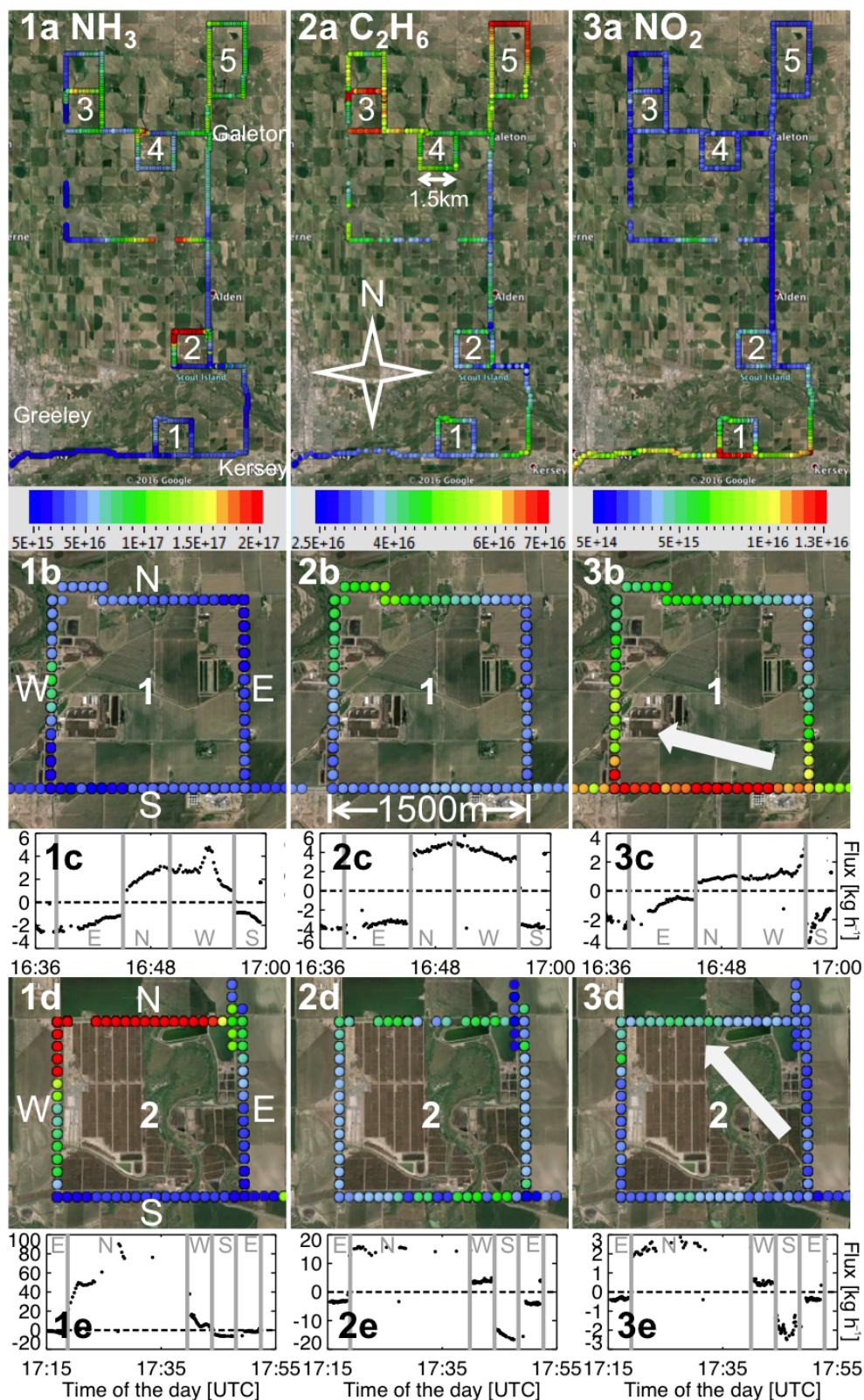


**Figure 8.** Zoom of the area east of Greeley, CO, with the RD11 drive track color coded by the VCD of (left column, 1)  $\text{NH}_3$ , (middle, 2)  $\text{C}_2\text{H}_6$  and (right, 3)  $\text{NO}_2$ . Row (a) shows the five sites of interest, (b) shows site 1 and (d) shows site 2 from Fig. 6. Rows (c) and (e) show a time series of the flux, calculated using Eq. (1); the arrows in (3b) and (3d) indicate the mean wind direction at each site. (Background image from Google Earth 2016.)

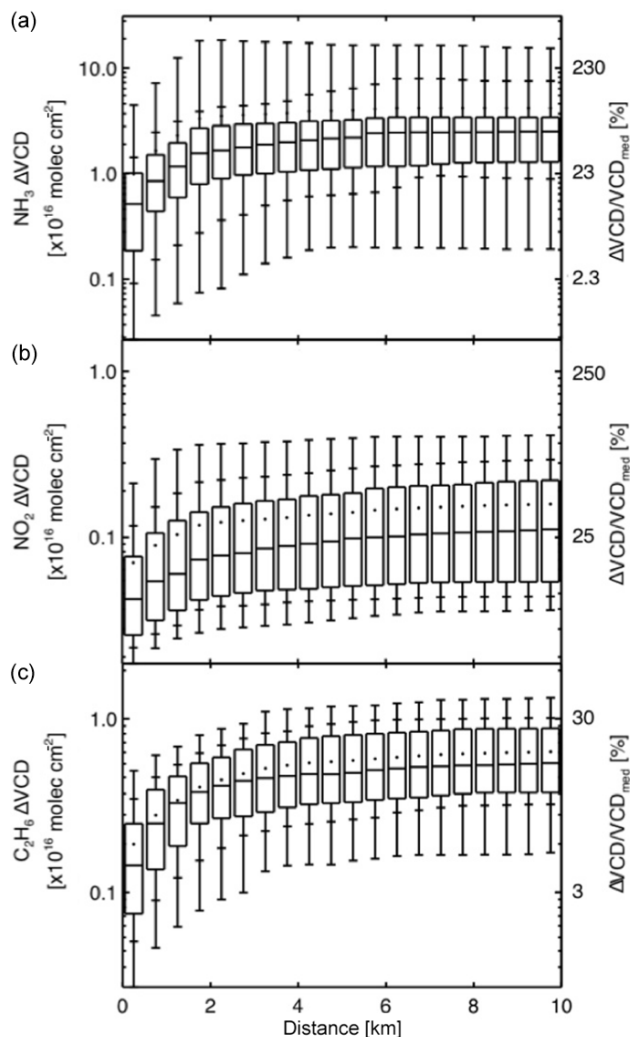


**Figure 9.** Structure functions of (a)  $\text{NH}_3$ , (b)  $\text{C}_2\text{H}_6$  and (c)  $\text{NO}_2$  using data from RD11 with a time constraint of 30 min for the time period of the five sites. The bin width is 500 m. Boxes mark 25th and 75th percentiles, the dot indicates the mean and the line inside the box marks the median. Dashes below and above the boxes indicate 5th, 15th, 85th and 95th percentile.

these error bars. The individual gas fluxes are discussed in the following three subsections.

### 3.3.1 $\text{NH}_3$ fluxes

For sites 1, 2 and 4, the dairy and cattle feedlots are a source of  $\text{NH}_3$  during both RDs. The emission flux in site 2 with the largest head count of cattle shows agreement of better than 10% for RD10 and RD11. The average flux is  $649 \pm 24 \text{ kgNH}_3 \text{ h}^{-1}$  for 54 044 cattle. This consistency between two days gives confidence that the uncertainty in the wind is conservatively estimated here. The average emission factor for site 2 is  $12.0 \pm 2.8 \text{ gNH}_3 \text{ h}^{-1} \text{ head}^{-1}$  for both days during daytime in the summer. The uncertainty here

combines the day-to-day variability and error in the wind (taken as  $30\%/\sqrt{2}$ ). For the dairy farm in site 4 we obtain  $11.4 \pm 3.5 \text{ gNH}_3 \text{ h}^{-1} \text{ head}^{-1}$ . The per head emission flux from the two samples at site 2 and one sample at site 4 can be pooled resulting in an average emission factor of  $11.8 \pm 2.1 \text{ gNH}_3 \text{ h}^{-1} \text{ head}^{-1}$ . The head count for site 1 was unknown but can be estimated based on the pooled per head emission. The average emission flux from site 1 of  $108 \text{ kg h}^{-1}$  corresponds to  $\sim 9200$  cattle. During RD11 the upwind effect influenced the observed VCD at site 4 and precluded quantification of a flux. This means the upwind flux was significant, and variability during the course of driving around the site may have influenced the observed flux. A comparison of the determined  $\text{NH}_3$  fluxes to literature values is given in Sect. 3.4.1.

### 3.3.2 $\text{NO}_2$ production rates

Soils are sources of  $\text{NO}_x$ , which is primarily emitted as  $\text{NO}$  as a result of microbial activity (Zörner et al., 2016).  $\text{NO}_2$  is subsequently produced from the reaction  $\text{NO} + \text{O}_3 \rightarrow \text{NO}_2 + \text{O}_2$  in the atmosphere. Both RDs consistently showed site 2 is a significant source of  $\text{NO}_x$ , with an average measured  $\text{NO}_2$  production rate of  $14.5 \text{ kg h}^{-1}$ . The difference in the  $\text{NO}_2$  emission flux from  $18 \text{ kg h}^{-1}$  during RD10 and  $11 \text{ kg h}^{-1}$  during RD11 may represent differences in wind speed. During RD10 the wind speed was approximately 1 to  $2 \text{ m s}^{-1}$  slower than on RD11 (compare Figs. 7 and S2), allowing for less time for  $\text{NO}$  into  $\text{NO}_2$  conversion during transport. The reaction rate constant for the above reaction is  $k = 3.0 \times 10^{-12} \times e^{-1500/T} \text{ cm}^3 \text{ molec}^{-1} \text{ s}^{-1}$  (Sander et al., 2006), which at a temperature of 300 K corresponds to a value for the rate constant of  $2.02 \times 10^{-14} \text{ cm}^3 \text{ molec}^{-1} \text{ s}^{-1}$  during our case studies. On RD10 and RD11  $\text{O}_3$  concentrations of 64 and 68 ppb at 19:00 and 18:00 UTC, respectively (Pierce, 2016), correspond to a  $\text{NO}$  lifetime of  $\sim 40 \text{ s}$  (66 ppbv  $\text{O}_3$ ). With wind speeds of  $\sim 4 \text{ m s}^{-1}$   $\text{NO}$  was converted into  $\text{NO}_2$  over a distance of  $\sim 160 \text{ m}$  (RD11). In particular, there is sufficient time to convert most of the  $\text{NO}$  emissions into  $\text{NO}_2$  within the CAFO area of  $1.6 \times 1.6 \text{ km}^2$ . To estimate the  $\text{NO}_2/\text{NO}$  ratio under photostationary state, we also need to consider the photochemical destruction of  $\text{NO}_2$  from the reaction  $\text{NO}_2 + \text{O}_2 \rightarrow (\text{h}\nu) \text{NO} + \text{O}_3$ . Assuming a typical photolysis frequency,  $J(\text{NO}_2)$ , as  $\sim 8 \times 10^{-3} \text{ s}^{-1}$ , the  $\text{NO}_2/\text{NO}$  ratio is 3.6, indicating that  $\sim 80\%$  of  $\text{NO}_x$  is abundant as  $\text{NO}_2$ . The average measured  $\text{NO}_2$  production rate thus corresponds to a  $\text{NO}_x$  emission rate of  $18.6 \pm 7.4 \text{ kg h}^{-1}$  for site 2. For a fraction of the nearby soil emission there may not be sufficient time to reach the photochemical steady state, but this fraction is likely small. We conclude that the observed  $\text{NO}_2$  is a lower limit for the overall  $\text{NO}_x$  production. The  $\text{NO}_x$  flux is compared to the emission inventory (EPA, 2015) in Sect. 3.4.2.

We are able to determine that the  $\text{NO}_x$  is coming from the feedlot soil rather than point sources such as diesel genera-

tors or trucks. Based on Gaussian plume modeling a source point that is at a distance of 1.7 km from the measurement location (greatest distance of downwind measurement to a potential diesel generator for the beef feedlot at site 2) can have dispersed horizontally up to 300 m. We measured NO<sub>2</sub> column enhancement over a distance greater ~ 1.4 km, indicating that the source of NO<sub>x</sub> is the entire feedlot area.

### 3.3.3 C<sub>2</sub>H<sub>6</sub> fluxes

C<sub>2</sub>H<sub>6</sub> has a relatively long atmospheric lifetime of about 2 months and is lost in the reaction with OH: OH + C<sub>2</sub>H<sub>6</sub> → C<sub>2</sub>H<sub>5</sub> + H<sub>2</sub>O. Assuming an OH concentration of  $8 \times 10^6$  molecules cm<sup>-3</sup> and taking the OH reaction rate constant of  $2.4 \times 10^{-13}$  cm<sup>3</sup> molec<sup>-1</sup> s<sup>-1</sup> (Sander et al., 2006), the lifetime of C<sub>2</sub>H<sub>6</sub> is 60 days, which gives rise to a Northern Hemisphere (NH) background VCD of, for example,  $3.1 \times 10^{16}$  molecules cm<sup>-2</sup> at Kiruna, Sweden (Angelbratt et al., 2011). C<sub>2</sub>H<sub>6</sub> VCD enhancements over the NH background are therefore expected to mix on regional scales and are subject to significant transport in the atmosphere. The RDs measured the lowest VCDs of C<sub>2</sub>H<sub>6</sub> in Boulder County, CO with its moratorium on fracking. Enhanced VCDs were observed throughout Weld County, CO, in areas with active ONG production. Using all 16 RDs, the median (minimum, maximum) VCDs in Boulder County and Weld County were 1.5 (0.5, 3.1) × 10<sup>16</sup> and 3.5 (1.0, 10) × 10<sup>16</sup> molecules cm<sup>-2</sup>, respectively. The influence from upwind sources makes the quantification of C<sub>2</sub>H<sub>6</sub> emission fluxes a bit more challenging. We consistently were able to quantify a positive emission flux out of site 1, as shown in Table 5. Site 1 was also influenced from upwind sources, but the mean C<sub>2</sub>H<sub>6</sub> flux was calculated as 63.5 kg h<sup>-1</sup> with an uncertainty of 29 kg h<sup>-1</sup>. The C<sub>2</sub>H<sub>6</sub> flux is compared to the emission inventory (EPA 2015) in Sect. 3.4.3.

## 3.4 Comparison with literature values

### 3.4.1 NH<sub>3</sub> fluxes from CAFO

We compare the NH<sub>3</sub> per head emission rate from cattle and dairy with literature values in Table 6. In Sect. 3.3.1 we calculated the emission rate of NH<sub>3</sub> for cattle to be  $11.8 \pm 2.1$  g h<sup>-1</sup> head<sup>-1</sup> based on the beef and dairy farm estimated capacity and observed NH<sub>3</sub> VCDs. Notably, it is not guaranteed that during the RD the feedlot was at maximum occupancy. If the occupancy was lower than the maximum occupancy, the value of  $11.8$  g h<sup>-1</sup> head<sup>-1</sup> would be a lower limit of the actual per head emission rate. The area of site 2 is mostly covered by two cattle feedlots, such that the likelihood of measuring NH<sub>3</sub> from another source such as fertilizers is low. The comparison with literature values in Table 6 shows that our per head emission factor of NH<sub>3</sub> is near the upper range of reported values and higher by a factor of 1.1 to 8.9. Plausible explanations may be due

to differences in environmental conditions such as air temperature, variations in the food and operation practices employed at CAFO outside of Colorado. An overview of location and conditions that were tested is given in Table 6. Generally the emission is higher in spring and summer when temperatures are warmer than in winter, when the emission is lower. However, the highest previously reported emission factor of 10.4 g h<sup>-1</sup> head<sup>-1</sup> was obtained under significantly colder temperatures (Bjorneberg et al., 2009), suggesting that factors other than temperature contribute to the significant variability among literature values.

Additionally we compare the NH<sub>3</sub> emission flux with the NEI 2011 emission inventory (EPA, 2015). The inventory has been formatted to a 3 km WRF-Chem grid, and the emissions for July 2011 are given as hourly intervals and do not distinguish between different source sectors. Agriculture is responsible for the major share of NH<sub>3</sub> emissions in the Colorado Front Range. For Fig. S4 the maximum emission flux from the diurnal profile in NEI 2011 was extracted corresponding to 0.73 kg km<sup>-2</sup> h<sup>-1</sup> at 20:00 UTC, in order to make a conservative comparison with the measured NH<sub>3</sub> emission rates. For comparison, the 16:00–22:00 UTC average NEI 2011 emission flux is 0.71 kg km<sup>-2</sup> h<sup>-1</sup>. We compare the emission flux of NH<sub>3</sub> in several ways. The first approach is to use Weld County, where the emission inventory suggests an average NH<sub>3</sub> flux of 0.36 kg km<sup>-2</sup> h<sup>-1</sup> for the maximum daytime emissions during summer. Based on our average per head emission factor, and a maximum head count of 535 766 cattle from beef and dairy feedlots in Weld County in 2014 (D. Bon, 2016, personal communication), the NH<sub>3</sub> emission flux is 0.63 kg km<sup>-2</sup> h<sup>-1</sup>. That means that the EPA (2011) inventory underestimates the NH<sub>3</sub> emission for the total county by about a factor of 2. Focusing on the area within Weld County, containing the five sites probed during our RDs, the inventory suggests the NH<sub>3</sub> emission flux is 0.73 kg km<sup>-2</sup> h<sup>-1</sup> compared to the NH<sub>3</sub> flux of 6.39 kg km<sup>-2</sup> h<sup>-1</sup> based on head count within the area. This represents an underestimation by a factor of about 10. The differences with the NEI are estimated conservatively here and could be lower limits if other NH<sub>3</sub> sources were located within the county, but not captured by our measurements, or if the CAFOs probed were not a maximum capacity. The emission inventory is from a few years prior to the RDs, and the total emission of the feedlots may have increased, as may have the number of feedlots within the grid cells. The 2007 Census of Agriculture for Weld County indicates 565 327 as number of cattle and calves, the 2012 Census indicates 501 446, and for 2014 the capacity was 535 766. Even if the number of feedlots within individual grid cells changed, the capacity did not change by more than 12 %, which does not describe the underestimation of NH<sub>3</sub> emission that we quantified. Finally, more case studies are needed for a firm assessment of the NEI in Colorado, despite the significant sample size of CAFOs, excellent reproducibility among different sites and on different days that we observe in this study.

**Table 6.** Comparison of NH<sub>3</sub> emission rates from cattle with literature values.

Location	Cattle	Number of cattle	Method	Ambient condition	NH <sub>3</sub> flux (g h <sup>-1</sup> head <sup>-1</sup> )	Reference
Colorado	Beef	54 044	Mobile SOF	August, 28 ± 3 °C	12.0 ± 2.8	This work
	Dairy	7450		August, 32 ± 2 °C	11.4 ± 3.5	
	Pooled	–		August, 30 ± 5 °C	11.8 ± 2.1	
Texas	Beef	50 000	Open-path laser	Summer/spring	6.25	Flesch et al. (2007)
Nebraska	Beef	6366	–	Summer/fall	6.79	Kissinger et al. (2007)
				Winter/spring	4.96	
Victoria, Australia	Beef	17 700	Closed-path gas analyzer	August, daytime	5.21	Denmead et al. (2008)
Queensland, Australia	Beef	16 800		August/September, daytime	3.12	
Texas	Beef	44 651	Acid gas washing samplers mounted on a tower	July/August	5.25 ± 0.33	Todd et al. (2008)
				January/February	2.81 ± 0.97	
Texas	Dairy	2000	Mobile chemiluminescence analyzer	July, 26 ± 1 °C	1.32 ± 0.81	Mukhtar et al. (2008)
				December, 6 ± 0.4 °C	0.71 ± 0.42	
Idaho	Dairy	700	Open-path FTS (OP/FTS)	January, –8 to –2 °C	1.66	Bjorneberg et al. (2009)
				March, –1 to –14 °C	10.4	
				June, 8 to 43 °C	7.92	
				September, 5 to 23 °C	6.25	
Idaho	Dairy	10 000	Photoacoustic gas monitors, OP/FTS	June/July/August, 16 to 24 °C	4.62 ± 0.83	Leytem et al. (2013)
				December/January, –8 to –5 °C	0.54 ± 0.11	
California	Dairy	–	Mobile wavelength modulation absorption spectroscopy	January, 9 to 20 °C	1.87 ± 0.40	Miller et al. (2015)
Colorado	Beef	22 000	Eddy covariance	November, –10 to 20 °C	2.64 ± 0.26	Sun et al. (2015b)

We conclude that using the NEI 2011 emission inventory in air quality models most likely underestimates the actual NH<sub>3</sub> emissions during FRAPPE by a factor of 2–10.

### 3.4.2 NO<sub>x</sub> emissions from CAFO

We have consistently observed significant NO<sub>x</sub> emissions from CAFO with a rate of 7.3 ± 2.9 kg km<sup>-2</sup> h<sup>-1</sup> from site 2, or 18.6 kg h<sup>-1</sup> during both RDs. No sharp plumes were observed downwind of the site (see Figs. 7c, 8-2d, and Figs. S2c, S3-2d). The NO<sub>2</sub> column enhancements closely resemble the area of cattle feeding operations, which suggests the observed NO<sub>x</sub> is emitted from microbial activity in the CAFO soils rather than a stationary combustion source. In order to assess the potential relevance of the enhanced soil emissions of NO<sub>x</sub> from CAFOs for the overall NO<sub>x</sub> emissions in Weld County, we determine the NO<sub>x</sub> production rate for cattle as 0.34 g h<sup>-1</sup> head<sup>-1</sup> from site 2. Notably, the fact that we did not observe NO<sub>x</sub> emissions from other sites is compatible with this assumption. At the feedlot in site 4 we were not able to obtain a reproducible flux on RD10 and RD11; instead, the emission was slightly positive on RD10 and negative on RD11 due to an upwind

plume affecting the measurements (see Table 5). Using the per head NO<sub>x</sub> flux as determined based on site 2, the NO<sub>x</sub> flux for site 4 would have been 2.5 kg h<sup>-1</sup> compared to the average NO<sub>x</sub> flux of 1.7 ± 0.5 kg h<sup>-1</sup> during RD10. There is thus reasonable agreement if the difference in the CAFO capacity is accounted for. Based on the total count of 533 766 cattle in Weld County and an area of 10 404 km<sup>2</sup> we obtain an average contribution from CAFO soil emissions of 0.018 kg km<sup>-2</sup> h<sup>-1</sup>. The inventory produces a NO<sub>x</sub> flux of 0.17 kg km<sup>-2</sup> h<sup>-1</sup> averaged over Weld County (EPA 2015), which includes emissions from urban areas. We conclude that the NO<sub>x</sub> source associated with enhanced microbial activity in CAFO soils could potentially contribute ~ 10 % to the overall NO<sub>x</sub> emissions of Weld County.

The contribution is even higher in the remote area of the five sites probed during the RDs. Here, the inventory produces an average NO<sub>x</sub> flux of 0.15 kg km<sup>-2</sup> h<sup>-1</sup>. Based on the total count of 224 469 cattle in the CAFOs distributed over the area of 414 km<sup>2</sup> shown in the bottom panel of Fig. S4, the NO<sub>x</sub> source from CAFO soils corresponds to 0.18 kg km<sup>-2</sup> h<sup>-1</sup>. We conclude that the CAFO soil emissions can double the NO<sub>x</sub> source in the inventory in the area probed by our case studies.

This potentially significant contribution of soil  $\text{NO}_x$  from CAFO is particularly relevant, because the photochemical  $\text{O}_3$  formation in the Colorado Front Range is  $\text{NO}_x$  limited. Missing sources of  $\text{NO}_x$  in the NEI directly translate into underestimates in the photochemical  $\text{O}_3$  production rate in the Front Range, which is an  $\text{O}_3$  non-attainment area. Very little quantitative information is currently available on  $\text{NO}_x$  emissions from CAFO. We did not make any attempts to retrieve NO from the CU mobile SOF spectra, which hold potential to complement the  $\text{NO}_2$  VCD observations in the future.

### 3.4.3 $\text{C}_2\text{H}_6$ emissions

We determined that the  $\text{C}_2\text{H}_6$  emission for site 1 is  $63.5 \pm 29 \text{ kg h}^{-1}$ . The NEI 2011 emission inventory (EPA, 2015) estimates the  $\text{C}_2\text{H}_6$  emission for that area as  $2.39 \text{ kg km}^{-2} \text{ h}^{-1}$ . Scaling our emission rate to the area of that one  $9 \text{ km}^2$  grid cell of the inventory, we obtain  $\sim 7 \text{ kg km}^{-2} \text{ h}^{-1}$  from site 1. While these measurements indicate the capability of mobile SOF to quantify elevated fluxes of  $\text{C}_2\text{H}_6$ , possibly from leaks, this flux is likely not representative of the greater area of the county. The CU mobile SOF  $\text{C}_2\text{H}_6$  measurements obtained on a regional scale are most useful if combined with a regional-scale chemistry transport model or inverse model to estimate the  $\text{C}_2\text{H}_6$  emissions in the Colorado Front Range. From in situ observations the ratio of  $\text{C}_2\text{H}_6 / \text{CH}_4$  for ONG emissions in Weld County has been measured as 18.4 % (A. Fried, personal communication, 2014), 11 % (A. Townsend-Small, personal communication, 2014) and 10 % (T. Yacovitch, personal communication, 2014). Based on the average ratio of  $13.1 \pm 4.6 \%$  and the emission flux for  $\text{C}_2\text{H}_6$ , the  $\text{CH}_4$  emission flux is  $39.2\text{--}82.7 \text{ kg km}^{-2} \text{ h}^{-1}$  at site 1.

### 3.5 Spatial variability

The structure function for the  $\text{NH}_3$ ,  $\text{NO}_2$  and  $\text{C}_2\text{H}_6$  VCDs are shown in Fig. 9. We applied a time constraint of 30 min to calculate the structure functions (compare Sect. 2.6, Eq. 3), in order to minimize changes in atmospheric state due to transport. Over the first few bins column differences in plumes are small due to measurements being in close vicinity of each other. At greater distances column differences increase and converge onto a plateau that is determined by the variability between plumes and background air masses.

During RD10 and RD11 we observed the highest spatial variability for  $\text{NH}_3$ , somewhat lower variability for  $\text{NO}_2$ , and the smallest variability for  $\text{C}_2\text{H}_6$  VCDs. The observed plateau values were  $2.52 \times 10^{16}$  for  $\text{NH}_3$ ,  $0.13 \times 10^{16}$  for  $\text{NO}_2$  and  $0.57 \times 10^{16}$  molecules  $\text{cm}^{-2}$  for  $\text{C}_2\text{H}_6$ , which correspond to 58.6, 32.5 and 16.3 % of the median VCD for  $\text{NH}_3$ ,  $\text{NO}_2$  and  $\text{C}_2\text{H}_6$ , respectively. These plateau values should be viewed as specific for our study area, and they may differ significantly for urban areas, where the sources may be more distributed.

**Table 7.** Variability length scale of  $\text{NH}_3$ ,  $\text{NO}_2$  and  $\text{C}_2\text{H}_6$ .

	$L_V$ (50 %) (km) <sup>a</sup>	$L_V$ (90 %) (km) <sup>b</sup>	$L_V$ (LOD) (km) <sup>c</sup>
$\text{NH}_3$	1.625	5.625	0.075
$\text{NO}_2$	1.825	5.525	1.725
$\text{C}_2\text{H}_6$	1.225	6.175	0.425

<sup>a</sup> Length at which 50 % of the variability with respect to the median VCD occurs. <sup>b</sup> Length at which 90 % of the variability with respect to the median VCD occurs. <sup>c</sup> Length scale at which the VCD difference is equal to the value of the LOD.

The precision of our  $\text{NH}_3$  and  $\text{C}_2\text{H}_6$  measurements, given in Table 4, determines how well we can resolve variability in VCDs. If the VCD difference is smaller than the measurement precision, then the VCD differences may be insignificant within our measurement precision. While the mobile SOF probed VCDs at spatial resolution of 5–19 m, we are able to resolve significant variability on spatial scales greater than 25 m for all gases. The variability length scales (see Sect. 2.6, Eq. 4) of  $\text{NH}_3$ ,  $\text{NO}_2$  and  $\text{C}_2\text{H}_6$  for 50 and 90 % variability as well as the length scale near the LOD are given in Table 7. The 50 and 90 % variability length scales are similar for all gases despite their different plateau values, with  $L_V$  (50 %) occurring at distances well below 2 km and  $L_V$  (90 %) occurring at distances near and below 6 km.

The feedlots in sites 1, 2 and 4 which are sources for  $\text{NH}_3$  have a minimum width of 400 m for site 1 and 4 and 800 m for site 2. Our results are thus consistent with the expected plume diameters in close vicinity to these sites.

The current satellites measuring  $\text{NH}_3$  have a horizontal resolution of  $5.3 \times 8.5$  (TES) and  $12 \times 25 \text{ km}^2$  (IASI). Satellites measuring  $\text{NO}_2$  have a horizontal resolution of  $13 \times 24$  (OMI),  $40 \times 80$  (GOME2) and  $15 \times 26 \text{ km}^2$  (SCIAMACHY). The expected resolution of TEMPO (Tropospheric Emissions: Monitoring of Pollution), to be launched in 2019, from geostationary orbit is  $2 \times 4.5 \text{ km}^2$ . We observe significant variability, >90 %, in VCDs at variability length scales smaller than  $\sim 6 \text{ km}$  for  $\text{NH}_3$  and  $\text{C}_2\text{H}_6$ , and  $\sim 13 \text{ km}$  for  $\text{NO}_2$  (Table 7). This indicates that satellites are able to quantify 10 % of the total variability in VCDs. Future satellites such as TEMPO and GEMS have a horizontal resolution that will begin to approach the scales over which  $\text{NO}_2$  VCDs vary by 50 % in the atmosphere, though some averaging from limited grid-size resolution can still be expected.

## 4 Conclusion and outlook

We describe the CU mobile SOF instrument, characterize it, and demonstrate first applications to characterize structure functions and quantify emission fluxes of  $\text{NH}_3$ ,  $\text{NO}_x$  and  $\text{C}_2\text{H}_6$ . The instrument can be extended to measure other trace gases that absorb at UV–vis–IR wavelengths, i.e., sulfur dioxide ( $\text{SO}_2$ ), nitric oxide (NO), nitrous

acid (HONO), hydrogen cyanide (HCN), acetylene (C<sub>2</sub>H<sub>2</sub>), methanol (CH<sub>3</sub>OH), formic acid (HCOOH), formaldehyde (HCHO), glyoxal (C<sub>2</sub>H<sub>2</sub>O<sub>2</sub>), ozone (O<sub>3</sub>), among others.

We conclude that mobile SOF measurements of trace gas VCDs are complementary to in situ observations, eliminate assumptions about vertical distributions and allow for a more direct comparison with satellites. Also, the FTS is well suited to detect typical VCDs in the Colorado Front Range with excellent signal to noise ratio. The NH<sub>3</sub>, NO<sub>2</sub> and C<sub>2</sub>H<sub>6</sub> VCDs were above the instrument detection limit in 99.98, 95.89 and 100 % of the spectra, respectively. The CU mobile SOF instrument line shape is not affected by changes in azimuth or elevation angles, providing robust spectral retrievals also while driving on dirt roads or around corners.

The total VCD error is 4.4 % for NH<sub>3</sub>, 6.7 % for C<sub>2</sub>H<sub>6</sub> and 5 % for NO<sub>2</sub> at high signal to noise ratio, and the accuracy is  $0.10 \times 10^{16}$  for NH<sub>3</sub> and  $0.13 \times 10^{16}$  molecules cm<sup>-2</sup> for C<sub>2</sub>H<sub>6</sub>. The error limiting the spectroscopic measurement is the cross section uncertainty. The uncertainty in the flux calculations is limited by the knowledge about the winds, consistent with earlier conclusions (Mellqvist et al., 2010). Determination of the spatial variability and structure function is not limited by the instrument precision, unless at very low distances shorter than 25 m. This is similar to earlier findings in situ data (Follette-Cook et al., 2015).

Significant variability in the VCDs is observed for all gases on scales smaller than 6 km, and we found 50 % of the VCD variability was at distances shorter than 2 km. Most of this variability happens on scales smaller than current ground pixel sizes of satellites. At the available spatial resolutions, satellites currently quantify less than 10 % of the observed VCD variability. Future missions from geostationary orbit, such as TEMPO, GEMS and Sentinel4, will have smaller ground pixels, which can resolve 10 to <50 % of the variability observed in the NO<sub>2</sub> VCDs.

A regional gradient was observed for C<sub>2</sub>H<sub>6</sub> between Boulder County and Weld County. The median, minimum and maximum C<sub>2</sub>H<sub>6</sub> VCDs were 2–3 times larger in Weld County, consistent with the active ONG extraction here and a moratorium on fracking in Boulder County (in 2014).

Emission fluxes for NH<sub>3</sub> during the summer day time are generally underestimated in the NEI 2011 emission inventory, as well as NO<sub>x</sub> emissions from CAFO soil. This indicates there are sources that have not been accounted for in the inventory. We determined that the per head emission of NH<sub>3</sub> during two summer days is underestimated by a factor of 2–10 than determined by other literature and the emission inventory. Emissions of NO<sub>x</sub> from microbiological activity in CAFO soils account for ~10 % of the total NO<sub>x</sub> emission in Weld County, CO, and can double the NO<sub>x</sub> source in the rural agricultural areas studied.

The CU mobile SOF instrument provides a versatile, efficient and robust tool to improve the statistics of emission fluxes of NH<sub>3</sub>, NO<sub>x</sub> and C<sub>2</sub>H<sub>6</sub> as there are no losses in sampling lines, study emissions of other gases and study vari-

ations in emissions with temperature, in different seasons, from point and area sources inside and outside of Colorado. The quality of the emission flux estimates benefits from independent wind measurements and closer attention to upwind effects in particular for C<sub>2</sub>H<sub>6</sub>. The airborne deployment of the CU mobile SOF instrument is planned for summer 2016 and has the potential to make mobile SOF measurements independent of roads, which is of interest to the studies in more complex terrain, such as of biomass burning events.

### List of primary chemicals and acronyms

C<sub>2</sub>H<sub>6</sub> – ethane  
 HCHO – formaldehyde  
 NH<sub>3</sub> – ammonia  
 NO<sub>2</sub> – nitrogen dioxide  
 NO<sub>x</sub> – sum of nitric oxide (NO) and NO<sub>2</sub>  
 CAFO – concentrated animal feeding operation  
 CLD – center to limb darkening  
 CU – University of Colorado  
 DOAS – differential optical absorption spectroscopy  
 DS-DOAS – direct-sun DOAS  
 EPA – Environmental Protection Agency  
 FRAPPE – Front Range Air Pollution and Photochemistry Experiment  
 FTS – Fourier transform spectrometer  
 HR-NCAR-FTS – high-resolution FTS at the National Center for Atmospheric Research  
 ILS – instrument line shape  
 InSb – indium antimonide  
 IR – infrared  
 LOD – limit of detection  
 MAX-DOAS – multi-axis DOAS  
 MCT – mercury cadmium telluride  
 NEI – National Emission Inventory  
 ONG – oil and natural gas  
 OPD – optical path difference  
 PBLH – planetary boundary layer height  
 RD – research drive  
 SOF – Solar Occultation Flux  
 UV-vis – ultraviolet–visible  
 VCD – vertical column density

### 5 Data availability

The CU mobile SOF data are available from the DISCOVER-AQ data archive: <http://www-air.larc.nasa.gov/cgi-bin/ArcView/discover-aq.co-2014?GROUND-MOBILE=1>. Specialized data such as the collocation experiment at NCAR and model wind output along the presented research drive track can be obtained from the authors upon request.

The Supplement related to this article is available online at doi:10.5194/amt-10-373-2017-supplement.

*Author contributions.* Rainer Volkamer designed research; Natalie Kille, Sunil Baidar, Ivan Ortega, Roman Sinreich and Rainer Volkamer conducted the measurements; Philip Handley and Owen R. Cooper helped during the field deployment; Owen R. Cooper, Frank Hase, James W. Hannigan and Gabriele Pfister added tools and expertise during analysis; Natalie Kille and Sunil Baidar analyzed the data; Natalie Kille and Rainer Volkamer prepared the manuscript with contributions from all co-authors.

*Competing interests.* The authors declare that they have no conflict of interest.

*Acknowledgements.* Financial support from Colorado Department for Public Health and Environment (CDPHE), State of Colorado contract 14 FAA 64390 and National Science Foundation (NSF) EAGER grant AGS-1452317 is gratefully acknowledged. The solar tracker was developed with support from a CIRES Energy Initiative seed grant. The authors thank Daniel Bon from CDPHE for providing the inventory of feedlot capacities during FRAPPE, Eric Nussbaumer for the SFIT4 software, Melanie Follette-Cook for sharing code and helpful discussions, and Tom Ryerson for coordinating research drives. Natalie Kille is recipient of a CIRES graduate fellowship. Rainer Volkamer is recipient of a KIT Distinguished International Scholar award. We acknowledge support by Deutsche Forschungsgemeinschaft and Open Access Publishing Fund of KIT. NCAR is sponsored by the NSF.

Edited by: M. Hamilton

Reviewed by: M. K. Sha and two anonymous referees

## References

- Ahmadov, R., McKeen, S., Trainer, M., Banta, R., Brewer, A., Brown, S., Edwards, P. M., de Gouw, J. A., Frost, G. J., Gilman, J., Helmig, D., Johnson, B., Karion, A., Koss, A., Langford, A., Lerner, B., Olson, J., Oltmans, S., Peischl, J., Pétron, G., Pichugina, Y., Roberts, J. M., Ryerson, T., Schnell, R., Senff, C., Sweeney, C., Thompson, C., Veres, P. R., Warneke, C., Wild, R., Williams, E. J., Yuan, B., and Zamora, R.: Understanding high wintertime ozone pollution events in an oil- and natural gas-producing region of the western US, *Atmos. Chem. Phys.*, 15, 411–429, doi:10.5194/acp-15-411-2015, 2015.
- Angelbratt, J., Mellqvist, J., Simpson, D., Jonson, J. E., Blumenstock, T., Borsdorff, T., Duchatelet, P., Forster, F., Hase, F., Mahieu, E., De Mazière, M., Notholt, J., Petersen, A. K., Raffalski, U., Servais, C., Sussmann, R., Warneke, T., and Vigouroux, C.: Carbon monoxide (CO) and ethane (C<sub>2</sub>H<sub>6</sub>) trends from ground-based solar FTIR measurements at six European stations, comparison and sensitivity analysis with the EMEP model, *Atmos. Chem. Phys.*, 11, 9253–9269, doi:10.5194/acp-11-9253-2011, 2011.
- Baidar, S., Volkamer, R., Alvarez, R., Brewer, A., Davies, F., Langford, A., Oetjen, H., Pearson, G., Senff, C., and Hardesty, R. M.: Combining Active and Passive Airborne Remote Sensing to Quantify NO<sub>2</sub> and O<sub>x</sub> Production near Bakersfield, CA, 2013, *British Journal for Environmental and Climate Change*, 3, 566–586, doi:10.9734/BJECC/2013/5740, 2013.
- Baidar, S., Kille, N., Ortega, I., Sinreich, R., Thomson, D., Hannigan, J., and Volkamer, R.: Development of a digital mobile solar tracker, *Atmos. Meas. Tech.*, 9, 963–972, doi:10.5194/amt-9-963-2016, 2016.
- Baum, K. A., Ham, J. M., Brunzell, N. A., and Coyne, P. I.: Surface boundary layer of cattle feedlots: Implications for air emissions measurement, *Agr. Forest Meteorol.*, 148, 1882–1893, doi:10.1016/j.agrformet.2008.06.017, 2008.
- Bertram, T. H., Heckel, A., Richter, A., Burrows, J. P., and Cohen, R. C.: Satellite measurements of daily variations in soil NO<sub>x</sub> emissions, *Geophys. Res. Lett.*, 32, L24812, doi:10.1029/2005GL024640, 2005.
- Bjorneberg, D. L., Leytem, A. B., Westermann, D. T., Griffiths, P. R., Shao, L., and Pollard, M. J.: Measurement of Atmospheric Ammonia, Methane, and Nitrous Oxide at a Concentrated Dairy Production Facility in Southern Idaho Using Open-Path FTIR Spectrometry, *T. ASABE*, 52, 1749–1756, doi:10.13031/2013.29137, 2009.
- Boersma, K. F., Jacob, D. J., Trainic, M., Rudich, Y., DeSmedt, I., Dirksen, R., and Eskes, H. J.: Validation of urban NO<sub>2</sub> concentrations and their diurnal and seasonal variations observed from the SCIAMACHY and OMI sensors using in situ surface measurements in Israeli cities, *Atmos. Chem. Phys.*, 9, 3867–3879, doi:10.5194/acp-9-3867-2009, 2009.
- Carslaw, D. C. and Beevers, S. D.: Estimations of road vehicle primary NO<sub>2</sub> exhaust emission fractions using monitoring data in London, *Atmos. Environ.*, 39, 167–177, doi:10.1016/j.atmosenv.2004.08.053, 2005.
- Chen, J., Viatte, C., Hedelius, J. K., Jones, T., Franklin, J. E., Parker, H., Gottlieb, E. W., Wennberg, P. O., Dubey, M. K., and Wofsy, S. C.: Differential column measurements using compact solar-tracking spectrometers, *Atmos. Chem. Phys.*, 16, 8479–8498, doi:10.5194/acp-16-8479-2016, 2016.
- Coheur, P.-F., Herbin, H., Clerbaux, C., Hurtmans, D., Wespes, C., Carleer, M., Turquety, S., Rinsland, C. P., Remedios, J., Hauglustaine, D., Boone, C. D., and Bernath, P. F.: ACE-FTS observation of a young biomass burning plume: first reported measurements of C<sub>2</sub>H<sub>4</sub>, C<sub>3</sub>HO, H<sub>2</sub>CO and PAN by infrared occultation from space, *Atmos. Chem. Phys.*, 7, 5437–5446, doi:10.5194/acp-7-5437-2007, 2007.
- Dammers, E., Palm, M., Van Damme, M., Vigouroux, C., Smale, D., Conway, S., Toon, G. C., Jones, N., Nussbaumer, E., Warneke, T., Petri, C., Clarisse, L., Clerbaux, C., Hermans, C., Lutsch, E., Strong, K., Hannigan, J. W., Nakajima, H., Morino, I., Herrera, B., Stremme, W., Grutter, M., Schaap, M., Wichink Kruit, R. J., Notholt, J., Coheur, P.-F., and Erisman, J. W.: An evaluation of IASI-NH<sub>3</sub> with ground-based Fourier transform infrared spectroscopy measurements, *Atmos. Chem. Phys.*, 16, 10351–10368, doi:10.5194/acp-16-10351-2016, 2016.

- de Foy, B., Lei, W., Zavala, M., Volkamer, R., Samuelsson, J., Mellqvist, J., Galle, B., Martínez, A.-P., Grutter, M., Retama, A., and Molina, L. T.: Modelling constraints on the emission inventory and on vertical dispersion for CO and SO<sub>2</sub> in the Mexico City Metropolitan Area using Solar FTIR and zenith sky UV spectroscopy, *Atmos. Chem. Phys.*, 7, 781–801, doi:10.5194/acp-7-781-2007, 2007.
- De Gouw, J. A., Te Lintel Hekkert, S., Mellqvist, J., Warneke, C., Atlas, E. L., Fehsenfeld, F. C., Fried, A., Frost, G. J., Harren, F. J. M., Holloway, J. S., Lefer, B., Lueb, R., Meagher, J. F., Parrish, D. D., Patel, M., Pope, L., Richter, D., Rivera, C., Ryerson, T. B., Samuelsson, J., Walega, J., Washenfelder, R. A., Weibring, P., and Zhu, X.: Airborne Measurements of Ethene from Industrial Sources Using Laser Photo-Acoustic Spectroscopy, *Environ. Sci. Technol.*, 43, 2437–2442, doi:10.1021/es802701a, 2009.
- Denmead, O. T., Chen, D., Griffith, D. W. T., Loh, Z. M., Bai, M., and Naylor, T.: Emissions of the indirect greenhouse gases NH<sub>3</sub> and NO<sub>x</sub> from Australian beef cattle feedlots, *Aust. J. Exp. Agr.*, 48, 213–218, 2008.
- Doyle, G. J., Tuazon, E. C., Graham, R. A., Mischke, T. M., Winer, A. M., and Pitts Jr., J. N.: Simultaneous concentrations of ammonia and nitric acid in a polluted atmosphere and their equilibrium relationship to particulate ammonium nitrate, *Environ. Sci. Technol.*, 13, 1416–1419, doi:10.1021/es60159a010, 1979.
- Environmental Protection Agency (EPA): 2011 National Emission Inventory version 2, 2015.
- EPA Handbook: Optical Remote Sensing for Measurement and Monitoring of Emissions Flux, edited by: Mikael, D. K., Office of Air Quality Planning and Standards, Air Quality Analysis Division Measurement Technology Group, Research Triangle, North Carolina, 27711, 2011.
- European Commission: Best Available Technique (BAT) Reference Document for the Refining of Mineral Oil and Gas: Joint Research Centre, Institute for Prospective Technological Studies, ISBN 978-92-79-46198-9, ISSN 1831-9424, doi:10.2791/010758, 2015.
- Fangmeier, A., Hadwiger-Fangmeier, A., Van der Eerden, L., and Jäger, H.-J.: Effects of Atmospheric Ammonia on Vegetation – A Review, *Environ. Pollut.*, 86, 43–82, doi:10.1016/0269-7491(94)90008-6, 1994.
- Finlayson-Pitts, B. J. and Pitts Jr., J. N.: Chemistry of the Upper and Lower Atmosphere, Academic Press, San Diego, CA, 882–886, 2000.
- Fischer, H., Birk, M., Blom, C., Carli, B., Carlotti, M., von Clarmann, T., Delbouille, L., Dudhia, A., Ehalt, D., Endemann, M., Flaud, J. M., Gessner, R., Kleinert, A., Koopman, R., Langen, J., López-Puertas, M., Mosner, P., Nett, H., Oelhaf, H., Perron, G., Remedios, J., Ridolfi, M., Stiller, G., and Zander, R.: MIPAS: an instrument for atmospheric and climate research, *Atmos. Chem. Phys.*, 8, 2151–2188, doi:10.5194/acp-8-2151-2008, 2008.
- Flesch, T. K., Wilson, J. D., Harper, L. A., Todd, R. W., and Cole, N. A.: Determining ammonia emissions from a cattle feedlot with an inverse dispersion technique, *Agr. Forest Meteorol.*, 144, 139–155, doi:10.1016/j.agrformet.2007.02.006, 2007.
- Follette-Cook, M. B., Pickering, K. E., Crawford, J. H., Duncan, B. N., Loughner, C. P., Diskin, G. S., Fried, A., and Weinheimer, A. J.: Spatial and temporal variability of trace gas columns derived from WRF/Chem regional model output: Planning for geostationary observations of atmospheric composition, *Atmos. Environ.*, 118, 28–44, doi:10.1016/j.atmosenv.2015.07.024, 2015.
- Franco, B., Hendrick, F., Van Roozendaal, M., Müller, J.-F., Stavrou, T., Marais, E. A., Bovy, B., Bader, W., Fayt, C., Hermans, C., Lejeune, B., Pinardi, G., Servais, C., and Mahieu, E.: Retrievals of formaldehyde from ground-based FTIR and MAX-DOAS observations at the Jungfraujoch station and comparisons with GEOS-Chem and IMAGES model simulations, *Atmos. Meas. Tech.*, 8, 1733–1756, doi:10.5194/amt-8-1733-2015, 2015.
- Fried, A., McKeen, S., Sewell, S., Harder, J., Henry, B., Goldan, P., Kuster, W., Williams, E., Baumann, K., Shetter, R., and Cantrell, C.: Photochemistry of formaldehyde during the 1993 Tropospheric OH Photochemistry Experiment, *J. Geophys. Res.*, 102, 6283–6296, doi:10.1029/96JD03249, 1997.
- Glatthor, N., von Clarmann, T., Stiller, G. P., Funke, B., Koukouli, M. E., Fischer, H., Grabowski, U., Höpfner, M., Kellmann, S., and Linden, A.: Large-scale upper tropospheric pollution observed by MIPAS HCN and C<sub>2</sub>H<sub>6</sub> global distributions, *Atmos. Chem. Phys.*, 9, 9619–9634, doi:10.5194/acp-9-9619-2009, 2009.
- Harris, D., Foufoula-Georgiou, E., Droegemeier, K. K., and Levit, J. J.: Multiscale statistical properties of a high resolution precipitation forecast, *J. Hydrometeorol.*, 2, 406–418, 2001.
- Harrison, J. J., Allen, N. D. C., and Bernath, P. F.: Infrared absorption cross sections for ethane (C<sub>2</sub>H<sub>6</sub>) in the 3 μm region, *J. Quant. Spectrosc. Radiat. Transf.*, 111, 357–363, doi.org/10.1016/j.jqsrt.2009.09.010, 2010.
- Hase, F., Blumenstock, T., and Paton-Walsh, C.: Analysis of the instrumental line shape of high-resolution Fourier transform IR spectrometers with gas cell measurements and new retrieval software, *Appl. Opt.*, 38, 3417–3422, doi:10.1364/AO.38.003417, 1999.
- Hase, F., Hannigan, J. W., Coffey, M. T., Goldman, A., Höpfner, M., Jones, N. B., Rinsland, C. P., and Wood, S. W.: Intercomparison of retrieval codes used for the analysis of high-resolution, ground-based FTIR measurements, *J. Quant. Spectrosc. Radiat. Transf.*, 87, 25–52, doi:10.1016/j.jqsrt.2003.12.008, 2004.
- Hase, F., Frey, M., Blumenstock, T., Groß, J., Kiel, M., Kohlhepp, R., Mengistu Tsidu, G., Schäfer, K., Sha, M. K., and Orphal, J.: Application of portable FTIR spectrometers for detecting greenhouse gas emissions of the major city Berlin, *Atmos. Meas. Tech.*, 8, 3059–3068, doi:10.5194/amt-8-3059-2015, 2015.
- Höpfner, M., Volkamer, R., Grabowski, U., Grutter, M., Orphal, J., Stiller, G., von Clarmann, T., and Wetzels, G.: First detection of ammonia (NH<sub>3</sub>) in the Asian summer monsoon upper troposphere, *Atmos. Chem. Phys.*, 16, 14357–14369, doi:10.5194/acp-16-14357-2016, 2016.
- Hristov, A. N., Hanigan, M., Cole, A., Todd, R., McAllister, T. A., Ndegwa, P. M., and Rotz, A.: Review: Ammonia emissions from dairy farms and beef feedlots, *Can. J. Anim. Sci.*, 91, 1–35, doi:10.4141/CJAS10034, 2011.
- Hutchinson, G. L., Mosier, A. R., and Andre, C. E.: Ammonia and Amine Emissions from a Large Cattle Feedlot, *J. Environ. Qual.*, 11, 288–293, doi:10.2134/jeq1982.00472425001100020028x, 1982.
- Ibrahim, O., Shaiganfar, R., Sinreich, R., Stein, T., Platt, U., and Wagner, T.: Car MAX-DOAS measurements around entire cities: quantification of NO<sub>x</sub> emissions from the cities of Mannheim

- and Ludwigshafen (Germany), *Atmos. Meas. Tech.*, 3, 709–721, doi:10.5194/amt-3-709-2010, 2010.
- IPCC: Climate Change 2013: The Physical Science Basis, Contribution of Working Group I to the Fifth Assessment Report of the Intergovernmental Panel on Climate Change, edited by: Stocker, T. F., Qin, D., Plattner, G.-K., Tignor, M., Allen, S. K., Boschung, J., Nauels, A., Xia, Y., Bex, V., and Midgley, P. M., Cambridge University Press, Cambridge, UK and New York, NY, USA, 2013.
- IUPAC: Compendium of Chemical Terminology, 2nd Edn. (the “Gold Book”), edited by: McNaught, A. D. and Wilkinson, A., Blackwell Scientific Publications, Oxford, doi:10.1351/goldbook, 1997.
- Jaeglé, L., Steinberger, L., Martin, R. V., and Chance, K.: Global partitioning of  $\text{NO}_x$  sources using satellite observations: Relative roles of fossil fuel combustion, biomass burning and soil emission, *Faraday Discuss.*, 130, 407–423, doi:10.1039/b502128f, 2005.
- Johansson, J. K. E., Mellqvist, J., Samuelsson, J., Offerle, B., Moldanova, J., Rappenglück, B., Lefer, B., and Flynn, J.: Quantitative measurements and modeling of industrial formaldehyde emissions in the Greater Houston area during campaigns in 2009 and 2011, *J. Geophys. Res.-Atmos.*, 119, 4303–4322, doi:10.1002/2013JD020159, 2014a.
- Johansson, J. K. E., Mellqvist, J., Samuelsson, J., Offerle, B., Lefer, B., Rappenglück, B., Flynn, J., and Yarwood, G.: Emission measurements of alkenes, alkanes,  $\text{SO}_2$ , and  $\text{NO}_2$  from stationary sources in Southeast Texas over a 5 year period using SOF and mobile DOAS, *J. Geophys. Res.-Atmos.*, 119, 1973–1991, doi:10.1002/2013JD020485, 2014b.
- Jones, E.: EPA Updates Emission Standards for Petroleum Refineries/First-ever fence-line monitoring requirements will protect nearby communities, available at: <https://yosemite.epa.gov/opa/admpress.nsf/0/D12EDC1C383ADF0385257ECF005B96B6> (last access: 8 June 2016), 2015.
- Kim, S.-W., McKeen, S. A., Frost, G. J., Lee, S.-H., Trainer, M., Richter, A., Angevine, W. M., Atlas, E., Bianco, L., Boersma, K. F., Brioude, J., Burrows, J. P., de Gouw, J., Fried, A., Gleason, J., Hilboll, A., Mellqvist, J., Peischl, J., Richter, D., Rivera, C., Ryerson, T., de Lintel Hekkert, S., Walega, J., Warneke, C., Weibring, P., and Williams, E.: Evaluations of  $\text{NO}_x$  and highly reactive VOC emission inventories in Texas and their implications for ozone plume simulations during the Texas Air Quality Study 2006, *Atmos. Chem. Phys.*, 11, 11361–11386, doi:10.5194/acp-11-11361-2011, 2011.
- Kissinger, W. F., Koelsch, R. K., Erickson, G. E., and Klopfenstein, T. J.: Characteristics of manure harvested from beef cattle feedlots, *Appl. Eng. Agric.*, 23, 357–365, 2007.
- Kleiner, I., Tarrago, G., Cottaz, C., Sagui, L., Brown, L. R., Poynter, R. L., Pickett, H. M., Chen, P., Pearson, J. C., Sams, R. L., Blake, G. A., Matsuura, S., Nemtchinov, V., Varanasi, P., Fusina, L., and Di Lonardo, G.:  $\text{NH}_3$  and  $\text{PH}_3$  line parameters: the 2000 HITRAN update and new results, *J. Quant. Spectrosc. Ra.*, 82, 293–312, doi:10.1016/S0022-4073(03)00159-6, 2003.
- Lei, W., Zavala, M., de Foy, B., Volkamer, R., Molina, M. J., and Molina, L. T.: Impact of primary formaldehyde on air pollution in the Mexico City Metropolitan Area, *Atmos. Chem. Phys.*, 9, 2607–2618, doi:10.5194/acp-9-2607-2009, 2009.
- Leytem, A. B., Dungan, R. S., Bjorneberg, D. L., and Koehn, A. C.: Greenhouse Gas and Ammonia Emissions from an Open-Freestall Dairy in Southern Idaho, *J. Environ. Qual.*, 42, 10–20, doi:10.2134/jeq2012.0106, 2013.
- Long, G. L. and Winefordner, J. D.: Limit of detection, A closer look at the IUPAC definition, *Anal. Chem.*, 55, 712A–724A, doi:10.1021/ac00258a001, 1983.
- Lou, Y., Zhang, Q., Wang, H., and Wang, Y.: Catalytic oxidation of ethylene and ethane to formaldehyde by oxygen, *J. Catal.*, 250, 365–368, doi:10.1016/j.jcat.2007.06.015, 2007.
- Mellqvist, J., Samuelsson, J., Johansson, J., Rivera, C., Lefer, B., Alvarez, S., and Jolly, J.: Measurements of industrial emissions of alkenes in Texas using the solar occultation flux method, *J. Geophys. Res.*, 115, D00F17, doi:10.1029/2008JD011682, 2010.
- Miller, D. J., Sun, K., Tao, L., Pan, D., Zondlo, M. A., Nowak, J. B., Liu, Z., Diskin, G., Sachse, G., Beyersdorf, A., Ferrare, R., and Scarino, A. J.: Ammonia and methane dairy emission plumes in the San Joaquin Valley of California from individual feedlot to regional scales, *J. Geophys. Res.-Atmos.*, 120, 9718–9738, doi:10.1002/2015JD023241, 2015.
- Mukhtar, S., Mutlu, A., Capareda, S. C., and Parneli, C. B.: Seasonal and Spatial Variations of Ammonia Emissions from an Open-Lot Dairy Operation, *J. Air Waste Manage.*, 58, 369–376, doi:10.3155/1047-3289.58.3.369, 2008.
- Nussbaumer, E. and Hannigan, J.: Infrared Working Group Retrieval Code, SFIT, available at: <https://wiki.ucar.edu/display/sfit4/Infrared+Working+Group+Retrieval+Code,+SFIT> (last access: 8 June 2016), 2014.
- Parrish, D. D. and Fehsenfeld, F. C.: Methods for gas-phase measurements of ozone, ozone precursors and aerosol precursors, *Atmos. Environ.*, 34, 1921–1957, doi:10.1016/S1352-2310(99)00454-9, 2000.
- Pierce, G.: Air Quality Reports, Colorado Air Quality Department of Public Health and Environment, available at: <http://www.colorado.gov/airquality/report.aspx>, last access: 8 June 2016.
- Raga, G. B., Baumgardner, D., Castro, T., Martinez-Arroyo, A., and Navarro-Gonzalez, R.: Mexico City air quality: a qualitative review of gas and aerosol measurements (1960–2000), *Atmos. Environ.*, 35, 4041–4058, doi:10.1016/S1352-2310(01)00157-1, 2001.
- Ramanathan, V. and Feng, Y.: Air pollution, greenhouse gases and climate change: Global and regional perspectives, *Atmos. Environ.*, 43, 37–50, doi:10.1016/j.atmosenv.2008.09.063, 2009.
- Rinsland, C. P., Dufour, G., Boone, C. D., Bernath, P. F., and Chiou, L.: Atmospheric Chemistry Experiment (ACE) measurements of elevated Southern Hemisphere upper tropospheric  $\text{CO}$ ,  $\text{C}_2\text{H}_6$ ,  $\text{HCN}$ , and  $\text{C}_2\text{H}_2$  mixing ratios from biomass burning emissions and long-range transport, *Geophys. Res. Lett.*, 32, L20803, doi:10.1029/2005GL024214, 2005.
- Rothman, L. S., Gordon, I. E., Barbe, A., Benner, D. C., Bernath, P. F., Birk, M., Boudon, V., Brown, L. R., Campargue, A., Champion, J.-P., Chance, K., Coudert, L. H., Dana, V., Devi, V. M., Fally, S., Flaud, J.-M., Gamache, R. R., Goldman, A., Jacquemart, D., Kleiner, I., Lacome, N., Lafferty, W. J., Mandin, J.-Y., Massie, S. T., Mikhailenko, S. N., Miller, C. E., Moazzen-Ahmadi, N., Naumenko, O. V., Nikitin, A. V., and Orphal, J.: The HITRAN 2008 molecular spectroscopic database, *J. Quant. Spectrosc. Ra.*, 110, 9, 533–572, doi:10.1016/j.jqsrt.2009.02.013, 2009.

- Sander, S. P., Friedl, R. R., Golden, D. M., Kurylo, M. J., Moortgat, G. K., Keller-Rudek, H., Wine, P. H., Ravishankara, A. R., Kolb, C. E., Molina, M. J., Finlayson-Pitts, B. J., Huie, R. E., and Orkin, V. L.: Chemical Kinetics and Photochemical Data for Use in Atmospheric Studies, Evaluation Number 15, JPL Publication 06-2, 2006.
- Schrader, B.: Infrared and Raman Spectroscopy, VCH, Weinheim, Germany, 1995.
- Shephard, M. W., Cady-Pereira, K. E., Luo, M., Henze, D. K., Pinder, R. W., Walker, J. T., Rinsland, C. P., Bash, J. O., Zhu, L., Payne, V. H., and Clarisse, L.: TES ammonia retrieval strategy and global observations of the spatial and seasonal variability of ammonia, *Atmos. Chem. Phys.*, 11, 10743–10763, doi:10.5194/acp-11-10743-2011, 2011.
- Shephard, M. W. and Cady-Pereira, K. E.: Cross-track Infrared Sounder (CrIS) satellite observations of tropospheric ammonia, *Atmos. Meas. Tech.*, 8, 1323–1336, doi:10.5194/amt-8-1323-2015, 2015.
- Streets, D. G., Canty, T., Carmichael, G. R., de Foy, B., Dickerson, R. R., Duncan, B. N., Edwards, D. P., Haynes, J. A., Henze, D. K., Houyoux, M. R., Jacob, D. J., Krotkov, N. A., Lamsal, L. N., Liu, Y., Lu, Z., Martin, R. V., Pfister, G. G., Pinder, R. W., Salawitch, R. J., and Wecht, K. J.: Emissions estimation from satellite retrievals: A review of current capability, *Atmos. Environ.*, 77, 1011–1042, doi:10.1016/j.atmosenv.2013.05.051, 2013.
- Sun, K., Cady-Pereira, K., Miller, D. J., Tao, L., Zondlo, M. A., Nowak, J. B., Neuman, J. A., Mikoviny, T., Müller, M., Wisthaler, A., Scarino, A. J., and Hostetler, C. A.: Validation of TES ammonia observations at the single pixel scale in the San Joaquin Valley during DISCOVER-AQ, *J. Geophys. Res.-Atmos.*, 120, 5140–5154, doi:10.1002/2014JD022846, 2015a.
- Sun, K., Tao, L., Miller, D. J., Zondlo, M. A., Shonkwiler, K. B., Nash, C., and Ham, J. M.: Open-path eddy covariance measurements of ammonia fluxes from a beef cattle feedlot, *Agr. Forest Meteorol.*, 213, 193–202, doi:10.1016/j.agrformet.2015.06.007, 2015b.
- Todd, R. W., Cole, N. A., Clark, R. N., Flesch, T. K., Harper, L. A., and Baek, B. H.: Ammonia emissions from a beef cattle feedyard on the southern High Plains, *J. Atmos. Environ.*, 42, 6797–6805, doi:10.1016/j.atmosenv.2008.05.013, 2008.
- Van Damme, M., Clarisse, L., Heald, C. L., Hurtmans, D., Ngadi, Y., Clerbaux, C., Dolman, A. J., Erisman, J. W., and Coheur, P. F.: Global distributions, time series and error characterization of atmospheric ammonia ( $\text{NH}_3$ ) from IASI satellite observations, *Atmos. Chem. Phys.*, 14, 2905–2922, doi:10.5194/acp-14-2905-2014, 2014.
- Van Roozendaal, M. and Fayt, C.: WinDOAS 2.1, 2001.
- Walker, J. T., Whitall, D. R., Robarge, W., and Paerl, H. W.: Ambient ammonia and ammonium aerosol across a region of variable ammonia emission density, *Atmos. Environ.*, 38, 1235–1246, doi:10.1016/j.atmosenv.2003.11.027, 2004.
- Xiao, Y., Logan, J. A., Jacob, D. J., Hudman, R. C., Yantosca, R., and Blake, D. R.: Global budget of ethane and regional constraints on US sources, *J. Geophys. Res.*, 113, D21306, doi:10.1029/2007JD009415, 2008.
- Zhang, R., Suh, I., Zhao, J., Zhang, D., Fortner, E. C., Tie, X., Molina, L. T., and Molina, M. J.: Atmospheric New Particle Formation Enhanced by Organic Acids, *Science*, 304, 1487–1490, doi:10.1126/science.1095139, 2004.
- Zhang, Z., Jimenez, J. L., Canagaratna, M. R., Allan, J. D., Coe, H., Ulbrich, I., Alfarra, M. R., Takami, A., Middlebrook, A. M., Sun, Y. L., Dzepina, K., Dunlea, E., Docherty, K., DeCarlo, P. F., Salcedo, D., Onasch, T., Jayne, J. T., Miyoshi, T., Shimojo, A., Hatakeyama, S., Takegawa, N., Kondo, Y., Schneider, J., Drewnick, F., Borrmann, S., Weimer, S., Demerjian, K., Williams, P., Bower, K., Bahreini, R., Cottrell, L., Griffin, R. J., Rautiainen, J., Sun, J. Y., Zhang, Y. M., and Worsnop, D. R.: Ubiquity and dominance of oxygenated species in organic aerosols in anthropogenically-influenced Northern Hemisphere midlatitudes, *Geophys. Res. Lett.*, 34, L13801, doi:10.1029/2007GL029979, 2007.
- Zörner, J., Penning de Vries, M., Beirle, S., Sihler, H., Veres, P. R., Williams, J., and Wagner, T.: Multi-satellite sensor study on precipitation-induced emission pulses of  $\text{NO}_x$  from soils in semi-arid ecosystems, *Atmos. Chem. Phys.*, 16, 9457–9487, doi:10.5194/acp-16-9457-2016, 2016.